1    **Compromised function of an ESCRT complex promotes endolysosomal escape of tau seeds**

2    **and propagation of tau aggregation**

3

4    **Authors:**

5    John J. Chen[1], Diane L. Nathaniel[1], Preethi Raghavan[2], Maxine Nelson[1,3], Ruilin Tian[1,4], Eric

6    Tse[1], Jason Y. Hong[1], Stephanie K. See[1,5], Sue-Ann Mok[1,§], Daniel R. Southworth[1,6], Lea T.

7    Grinberg[6], Jason E. Gestwicki[1,8], Manuel D. Leonetti[2], Martin Kampmann[1,2,6,*]

8

9    **Affiliations:**

10    [1]Institute for Neurodegenerative Diseases, University of California, San Francisco, CA 94158,

11    USA

12    [2]Chan Zuckerberg Biohub, San Francisco, CA 94158, USA

13    [3]Biomedical Sciences Graduate Program, University of California, San Francisco, CA 94158,

14    USA

15    [4]Biophysics Graduate Program, University of California, San Francisco, CA 94158, USA

16    [5]Graduate Program in Chemistry and Chemical Biology, University of California, San Francisco,

17    CA 94158, USA

18    [6]Department of Biochemistry and Biophysics, University of California, San Francisco, CA

19    94158, USA

20    [7]Department of Neurology, University of California, San Francisco, CA 94158, USA

21    [8]Department of Pharmaceutical Chemistry, University of California, San Francisco, CA 94158,

22    USA

23    [§] Current affiliation: Department of Biochemistry, University of Alberta, Edmonton, AB,

24    Canada, T6G 2H7

25

26    *Correspondence to: martin.kampmann@ucsf.edu

27 **ABSTRACT**

28 Intercellular propagation of protein aggregation is emerging as a key mechanism in the

29 progression of several neurodegenerative diseases, including Alzheimer's Disease and

30 frontotemporal dementia. However, we lack a systematic understanding of the cellular pathways

31 controlling prion-like propagation. To uncover such pathways, we performed CRISPR

32 interference (CRISPRi) screens in a human cell-based model of propagation of tau aggregation.

33 Our screens uncovered that knockdown of components of the ESCRT-III machinery, namely

34 CHMP6, or CHMP2A in combination with CHMP2B (a gene linked to familial frontotemporal

35 dementia), promote propagation of tau aggregation. We found that knockdown of these genes

36 caused damage to endolysosomal membranes, consistent with a role for the ESCRT pathway in

37 endolysosomal membrane repair. Leakiness of the endolysosomal compartment significantly

38 enhanced prion-like propagation of tau aggregation, likely by making tau seeds more available to

39 pools of cytoplasmic tau. Together, these findings suggest that endolysosomal escape is a critical

40 step in tau propagation.

41

42

43 **INTRODUCTION**

44 Neurodegenerative diseases are one of the most pressing challenges facing humanity. A

45 formidable roadblock to the development of effective therapies is our incomplete understanding

46 of the underlying molecular and cellular mechanisms. A major breakthrough was the discovery

47 that scrapie, an infectious neurodegenerative disease, is caused by the cell-to-cell propagation of

48 protein aggregates via "prion" forms of the protein (Prusiner, 1982). In this process, a prion seed

49 converts healthy, native proteins to adopt an aggregated, prion conformer. More recently,

50 findings from numerous, independent studies support the hypothesis that prion-like propagation

51 also underlies common, non-infectious neurodegenerative diseases, such as Alzheimer's Disease

52 (AD) (recently reviewed in (Vaquer-Alicea & Diamond, 2019)). However, the mechanisms that

53 control aggregate uptake and propagation remain to be fully elucidated, especially in those

54 diseases that involve cytoplasmic proteins. A systematic understanding of these mechanisms is

55 important, both for the development of therapeutics and for furthering our understanding of why

56 specific neuronal subtypes and brain regions are especially susceptible to specific diseases.

57    Of particular interest to us are the mechanisms controlling propagation of aggregated

58    forms of the protein tau. Tau aggregation is one of the hallmarks of AD and the levels of

59    aggregated tau correlate with cognitive deficits and neuronal loss (Gomez-Isla et al., 1997; Berg

60    et al., 1998; Giannakopoulos et al., 2003; Bejanin et al., 2017). Beyond AD, tau aggregation also

61    defines a number of other neurodegenerative diseases, collectively termed tauopathies, some of

62    which are caused by familial point mutations in tau (Wang & Mandelkow, 2016).

63    Propagation of tau aggregation can be modeled in cultured HEK293 cells that express

64    fluorescently tagged versions of tau, as first established by the Diamond lab (Frost et al., 2009).

65    In this system, addition of aggregated tau seeds to the culture media causes the fluorescently

66    tagged tau in the cells to convert from a diffuse, soluble form to aggregated puncta. This cell-

67    based model has enabled the characterization of tau species with seeding activity from patient

68    brains (Mirbaha et al., 2015), and the creation of a minimal synthetic tau that retains seeding

69    capability (Stöhr et al., 2017). Furthermore, cell-based models can also be used as a biosensor to

70    detect and propagate distinct prion strains of tau from different tauopathies (Sanders et al., 2014;

71    Kaufman et al., 2016; Woerman et al., 2016). Importantly, seeding of tau aggregation in the cell-

72    based model is predictive of *in vivo* seeding in a mouse model (Holmes et al., 2014).

73    In addition to their utility as "biosensors" for tau aggregates with prion properties, cell-

74    based models can also be used to elucidate cellular pathways that control propagation of tau

75    aggregation. Previous work from others and us leveraged cell-based models to uncover

76    mechanisms that mediate tau uptake into cells (Frost et al., 2009; Holmes et al., 2013; Rauch et

77    al., 2018; Stopschinski et al., 2018). In those studies, binding of tau to specific cell-surface

78    heparan sulfate proteoglycans was found to mediate cellular uptake. These results were validated

79    in human iPSC-derived neurons and mouse brain slices (Rauch et al., 2018), supporting the

80    physiological relevance of the cell-based model.

81    While these studies established the mechanism for tau uptake, the downstream cellular

82    pathways controlling propagation of tau aggregation have not been systematically characterized.

83    We hypothesized that tau aggregation in the cytosol would be influenced by multiple cellular

84    pathways, including those controlling trafficking of tau seeds through the endolysosomal

85    pathway, localization of tau seeds to the cytosol, templated aggregation of soluble tau, and

86    clearance of tau aggregates (**Fig. 1A**).

87      To uncover relevant cellular pathways downstream of tau uptake, we here combine our

88      CRISPR interference-based genetic screening approach (Gilbert et al., 2014; Kampmann, 2018)

89      with a cell-based model of tau aggregation using fluorescence resonance energy transfer (FRET).

90      Using this approach, we uncover endolysosomal escape of tau seeds as a critical step in the

91      propagation of tau aggregation. Defects in the ESCRT machinery compromise endolysosomal

92      integrity, thereby promoting the escape of tau seeds from endolysosomal compartments and

93      accelerating subsequent templating of tau aggregation in the cytosol. These findings provide

94      insight into the mechanisms of tau trafficking and suggest a source for new potential therapeutic

95      targets.

96

97

98      **RESULTS**

99

100     **Cell-based model of prion-like propagation of tau aggregation**

101     We established a cell-based model to monitor the prion-like propagation of tau aggregation in

102     HEK293T cells. Such a model had previously been pioneered by the Diamond lab (Frost et al.,

103     2009) and adapted for flow cytometry using a FRET-based strategy to monitor tau aggregation

104     (Kfoury et al., 2012). In this FRET-based strategy, two versions of the tau repeat domain (RD)

105     containing disease-associated P301L and V337M mutations are expressed as fusions with either

106     the FRET donor CFP or the FRET acceptor YFP. When exposed to tau fibrils from recombinant

107     or cell/brain-derived lysate sources, the CFP and YFP tags are brought into close proximity,

108     enabling FRET. We generated a reporter line following a similar strategy (**Fig. 1B**). Instead of

109     the CFP-YFP FRET pair, we used Clover2 and mRuby2, since proteins of this type had been

110     shown to have a very high dynamic range for FRET, with a high Förster radius (Lam et al.,

111     2012). We selected a monoclonal line for optimal expression and dynamic range of the FRET

112     signal.

113
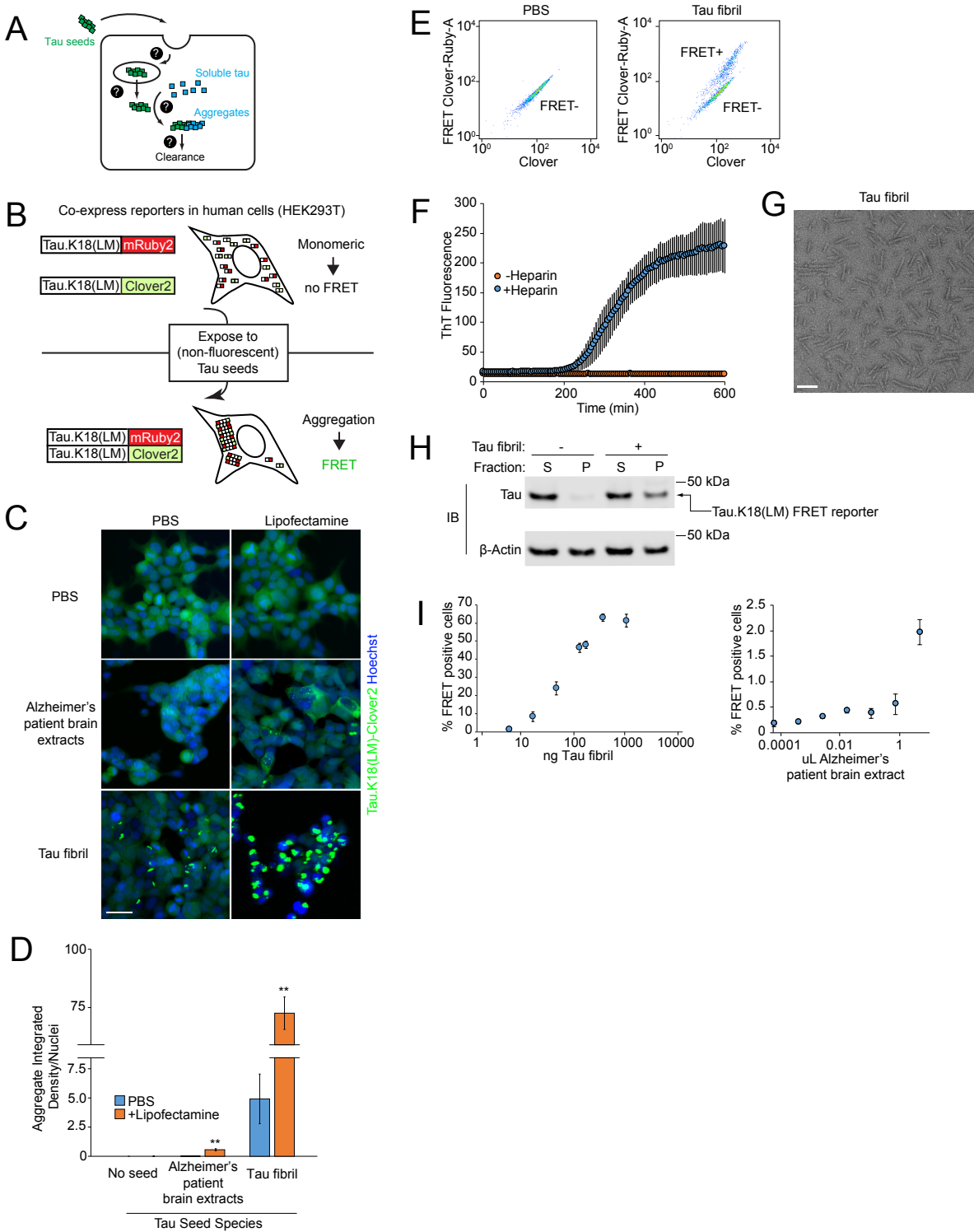
114

115    **Figure 1 – legend overleaf**

116 **Figure 1 – Tau seeds induce tau aggregation in a FRET-based reporter cell line**
117 (**A**) Overview of cellular processes that may control the prion-like tau propagation and aggregation.
118 Question marks represent unknown cellular mechanisms. (**B**) Schematic representation of the FRET-
119 based reporter assay to monitor tau aggregation in HEK293T cells. In the absence of tau seeds,
120 fluorescently labeled tau.K18(LM) is monomeric. Exposure to non-fluorescent tau seeds induces
121 aggregation of the reporter, which can be measured by the formation of tau aggregates by fluorescence
122 microscopy or an increase in FRET intensity by flow cytometry. (**C**) Induction of fluorescent tau
123 aggregates in FRET reporter cell line. Representative images of cells treated with PBS (top row),
124 Alzheimer's patient brain extracts after 5 days (*second row*), or fibrils of recombinant human 0N4R tau
125 after 2 days (*third row*). For each tau seed, each condition is complexed with (*right column*) or without
126 (*left column*) lipofectamine. Nuclei were counter-stained with Hoechst 33342. Scale bar = 50 μm (**D**)
127 Comparison of intracellular fluorescent tau aggregates from images in **Fig. 1C**. Integrated density
128 quantification of fluorescent tau aggregates seeded with various tau seeds complexed with *(blue)* or
129 without (*orange*) lipofectamine were quantified and divided by total nuclei per image. n=3 technical
130 replicates (with at least 50 nuclei per image), error bars represent standard deviation, * P<0.05, ** P<0.01
131 (two-tailed Student's t test for comparison to PBS (no lipofectamine) control for each tau seeding
132 condition). (**E**) Representative flow cytometry plot of FRET reporter cells after 2 day treatment with PBS
133 (*left*) or tau fibrils (*right*). (**F**) Incubation of recombinant 0N4R tau with heparin and constant agitation at
134 37° C induces fibrillization. Fibrillization is monitored using an increase in Thioflavin T fluorescence (ex:
135 440 nm, em: 485 nm), which occurs in the presence (blue) of heparin (10 μg/mL), but not in the absence
136 (orange) of heparin. Error bars represent standard deviation from n=3 technical replicates. (**G**)
137 Representative negative stain electron micrograph of tau fibrils. Scale bar = 100 nm (**H**) Lysates from
138 FRET reporter cells treated with PBS or tau fibrils for 2 days were fractionated at 1000xg into soluble (S)
139 or pellet (P) fractions, and subjected to SDS-PAGE and immunoblotting using antibodies against tau and
140 β-actin. (**I**) Quantification of % FRET positive cells using flow cytometry across concentration ranges of
141 tau fibrils (*left*) or human Alzheimer's patient brain extracts (*right*). Error bars represent standard
142 deviation for n=3 technical replicates.
143

144       In the absence of seeding, these cells showed diffuse intracellular fluorescence without

145 visible aggregates when monitored by fluorescence microscopy (**Fig. 1C,D**) and they appeared

146 as a single population when FRET levels are monitored by flow cytometry (**Fig. 1E**). In contrast,

147 exposure of these cells to extracts from AD patient brains caused the tau reporter constructs to

148 aggregate, as reflected by formation of fluorescent puncta (**Fig. 1C,D**). However, seeded

149 aggregation with brain-derived tau required co-incubation with lipofectamine 2000 (here referred

150 to as lipofectamine) to achieve modest aggregation (**Fig. 1C,D**), consistent with reports from

151 other groups (Holmes et al., 2014; Sanders et al., 2014; Woerman et al., 2016).

152       Our goal was to eliminate the use of lipofectamine, because the use of a lipocationic

153 carrier may bypass physiologically relevant uptake or trafficking pathways. Accordingly, we

154 purified monomeric 6xHis-tagged 0N4R human tau from *E. coli* and induced fibrillization with

155 heparin, which we monitored by an increase in thioflavin T fluorescence (**Fig. 1F**) and by

156 negative stain electron microscopy (**Fig. 1G**). We found that treatment of our FRET reporter

157 cells with these tau fibrils caused robust formation of aggregates, even in the absence of

6

158  lipofectamine. This activity was confirmed using multiple criteria, including formation of puncta

159  by fluorescence microscopy (**Fig. 1C,D**), appearance of a FRET-positive population by flow

160  cytometry (**Fig. 1E**), and biochemical characterization of tau in the insoluble fraction (**Fig. 1H**).

161  Finally, we tested the effects of increasing concentrations of tau fibrils on our FRET-based

162  reporter. We found that 6xHis-tagged fibrils robustly triggered tau aggregation in a dose-

163  dependent manner across nearly 2 orders of magnitude in concentration in the absence of

164  lipofectamine, as quantified by the percentage of FRET positive cells (**Fig. 1I**). Brain lysates also

165  produced an increase in FRET-positive cells, although the magnitude was more modest.

166  Together, these features make our FRET-based model suitable for use in a genetic screen to

167  identify cellular factors that control prion-like propagation of tau aggregation.

168

169  **Genetic screen to identify cellular factors that control prion-like propagation of tau**

170  **aggregation**

171  In order to identify cellular factors that control propagation of tau aggregation (**Fig. 1A**), we

172  conducted a CRISPR-interference (CRISPRi)-based genetic screen (**Fig. 2A**). First, we

173  transduced the reporter cell line described above with a lentiviral expression construct for a

174  catalytically inactive Cas9-BFP-KRAB (dCas9-BFP-KRAB) fusion protein. dCas9-BFP-KRAB

175  can be directed by small guide RNAs (sgRNAs) to silence a gene of interest (Gilbert et al.,

176  2013), enabling massively parallel genetic screens in mammalian cells (Gilbert et al., 2014). We

177  then transduced the cells with pooled sgRNA libraries that target protein homeostasis factors,

178  which we designed specifically for this study based on the rationale that protein homeostasis

179  factors were likely to control or modulate tau aggregation and clearance. These libraries target

180  2,949 genes encoding genes that function in autophagy, protein folding, or the ubiquitin-

181  proteasome system with at least five independent sgRNAs for each gene, plus 750 non-targeting

182  control sgRNAs. Cells transduced with these libraries were exposed to recombinant tau fibrils at

183  concentrations that would yield FRET positive cells at 50% of the maximum percentage of

184  FRET positive cells (**Fig. 1I**), thereby maximizing the dynamic range for detecting cellular

185  factors that either increase or decrease tau aggregation. FRET negative and FRET positive cell

186  populations were separated by FACS, collecting sufficient numbers of cells from each

187  population for an average 1000x representation (cells per sgRNA elements in the library).

188  Genomic DNA was isolated and the locus encoding the sgRNAs was PCR-amplified.

189 Frequencies for each sgRNA in each population were determined by next generation sequencing.

190 We evaluated genes for the effect their knockdown had on the formation of tau aggregates

191 (**Table S1**) using our previously described bioinformatics pipeline (Kampmann et al., 2013;

192 Gilbert et al., 2014; Kampmann et al., 2014; Tian et al., 2019).



193
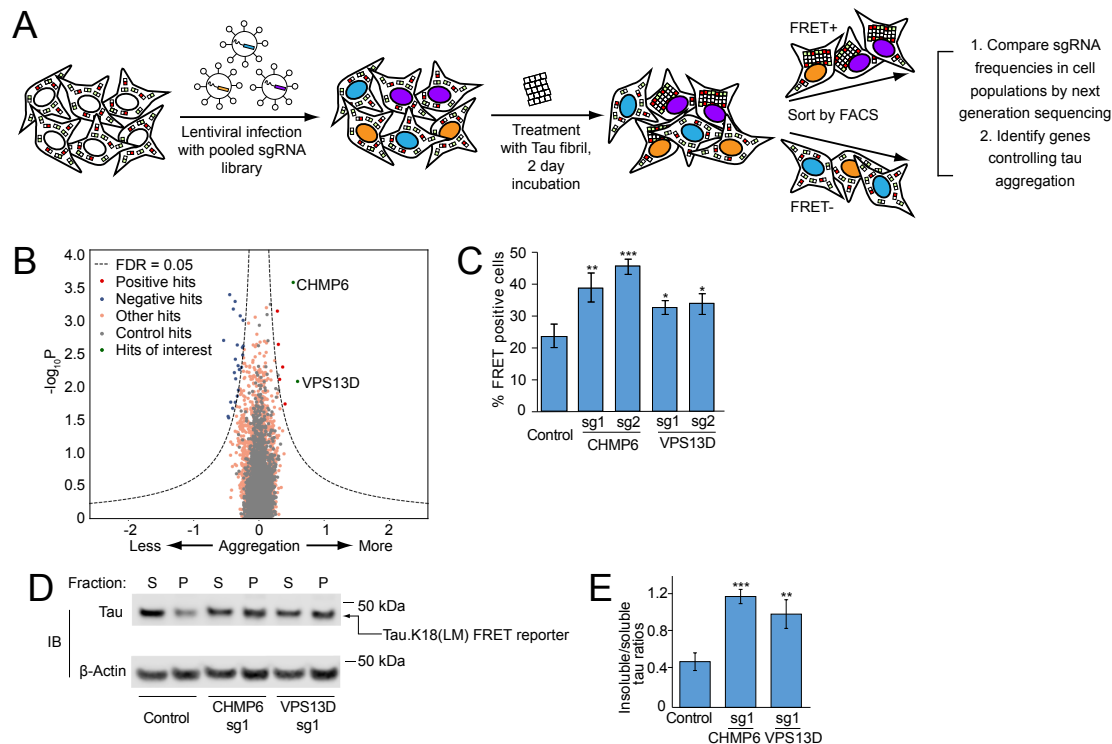
**Figure 2 – CRISPRi screen for cellular factors controlling tau aggregation**
194 (**A**) Strategy for pooled FRET-based CRISPRi screen. FRET reporter cells stably expressing the CRISPRi
195 machinery (dCas9-BFP-KRAB) were transduced with pooled lentiviral expression libraries of sgRNAs
196 targeting proteostasis genes. Following transduction and selection, cells were treated with tau fibrils and
197 incubated for 2 days. Cells were detached and sorted into FRET negative and positive populations by
198 Fluorescence-Activated Cell Sorting (FACS). sgRNA-encoding cassettes were amplified from genomic
199 DNA of the cell populations and their frequencies were quantified using next generation sequencing to
200 identify genes that control tau aggregation. (**B**) Volcano plot summarizing phenotypes and statistical
201 significance (by our MAGeCK-iNC pipeline, see Materials and Methods) of the genes targeted by the
202 sgRNA libraries. Non-targeting sgRNAs were randomly grouped into negative control "quasi-genes"
203 (grey dots) to derive an empirical false-discovery rate (FDR). Hit genes that passed an FDR < 0.05
204 threshold are shown in blue (knockdown decreases aggregation) or red (knockdown increases
205 aggregation), other genes are shown in orange. Two hit genes of interest are shown in green and labeled.
206 (**C-E**) Validation of hit genes CHMP6 and VPS13D. FRET reporter cells transduced with individual
207 sgRNAs targeting two hit genes or a non-targeting control sgRNA, and 5 days after transduction treated
208 for 2 days with tau fibrils. (C) % of FRET positive cells was quantified by flow cytometry. Error bars
209 represent standard deviation of n=3 technical replicates. *P<0.05, **P<0.01, ***P<0.001 (two-tailed
210 Student's t test for comparison to the non-targeting control sgRNA). (D) Representative immunoblot for
211 the tau-fluorescent protein construct in the soluble and insoluble fractions as in Fig. 1H. (E)
212 Quantification of insoluble/soluble tau ratios from immunoblots in Fig 2D. Error bars represent standard
213 deviation for n=3 biological replicates. P<0.05, **P<0.01, ***P<0.001 (two-tailed Student's t test for
214 comparison to the non-targeting control sgRNA).

8

216

217     Two genes stood out for the strong enhancement of tau aggregation by their knockdown:

218     CHMP6 and VPS13D (**Fig. 2B**). We decided to prioritize these two genes for further

219     characterization, since both are related to genes implicated in neurodegenerative diseases.

220     CHMP6 is part of the Endosomal Sorting Complex Required for Transport (ESCRT)-III

221     complex, which is required for numerous cellular processes involving membrane remodeling

222     (Hurley, 2015). Mutations in the ESCRT-III component CHMP2B cause familial frontotemporal

223     lobar dementia (FTD) and have been shown to cause endolysosomal defects (Urwin et al., 2010;

224     Clayton et al., 2015).

225     The *VPS13* protein family is comprised of four closely-related proteins, *VPS13A-D*

226     (Velayos-Baeza et al., 2004). VPS13 family proteins are localized at various inter-organelle

227     membrane contact sites and facilitates non-vesicular lipid transport (Kumar et al., 2018; Yeshaw

228     et al., 2019). Interestingly, mutations *VPS13D* are associated with recessive ataxia (Seong et al.,

229     2018). Previously, *VPS13A* and *VPS13C* mutations have been associated with a Huntington's-

230     like syndrome (Chorea-Acanthocytosis) (Rampoldi et al., 2001; Ueno et al., 2001) and

231     Parkinson's disease (Lesage et al., 2016), respectively.

232     To confirm these screening hits, we cloned 2 individual sgRNAs each targeting CHMP6

233     and VPS13D, and confirmed target knockdown by qPCR (**Table S2**). Using these sgRNAs, we

234     validated the effect of CHMP6 and VPS13D knockdown on tau aggregation by flow cytometry

235     (**Fig. 2C**) and biochemical solubility assay (**Fig. 2D, E**).

236

237     **CHMP6 knockdown accelerates tau aggregation following tau seed uptake**

238     We next investigated the mechanism by which knockdown of CHMP6 and VPS13D might affect

239     tau aggregation. First, we excluded the possibility that knockdown of these genes alters the levels

240     of our tau reporter (**Fig. 3A**). Since we previously identified factors controlling cellular uptake of

241     tau (Rauch et al., 2018), we tested whether knockdown of CHMP6 and VPS13D impacted the

242     uptake of tau fibrils. However, we found that knockdown of the genes did not impact tau fibril

243     uptake (**Fig. 3B**), suggesting that their impact on tau aggregation is mediated downstream of seed

244     uptake.

245

246
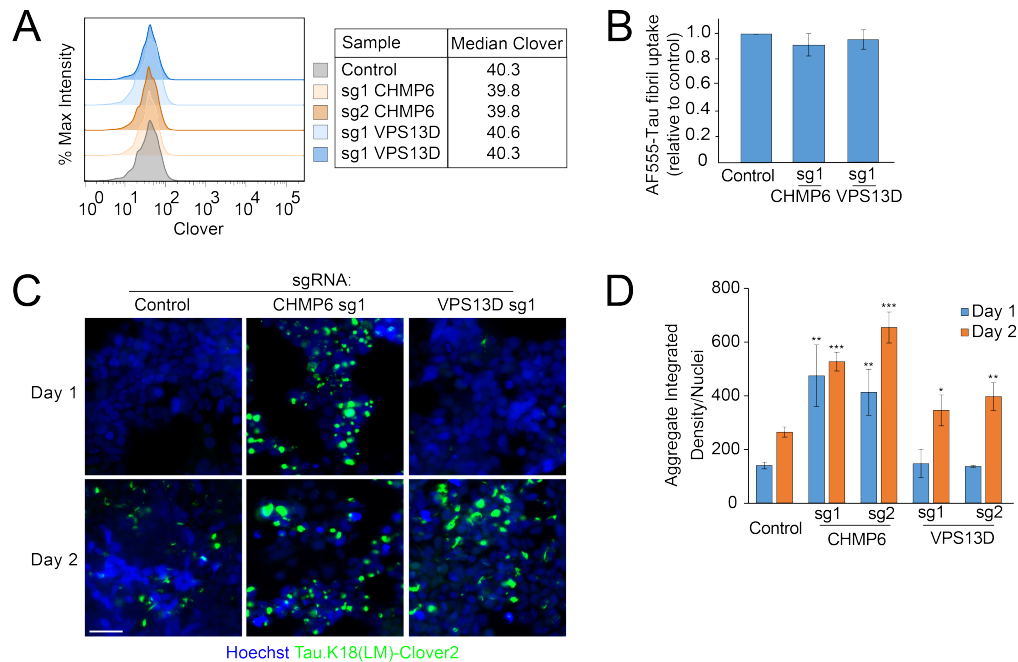
**Figure 3 – CHMP6 knockdown accelerates the prion-like propagation of tau aggregation**
FRET reporter cells or CRISPRi-HEK293T cells were transduced with individual sgRNAs targeting CHMP6 or VPS13D, or a non-targeting control sgRNA, and characterized for different phenotypes 5 days after transduction (**A**) Knockdown of CHMP6 and VPS13D does not impact steady state levels of the tau-Clover2 construct in FRET reporter cells, as quantified by flow cytometry. (**B**) Individual gene knockdown does not impact uptake of tau fibrils. CRISPRi HEK293T cells were incubated with AF555-labeled tau fibrils for 1 hour at 37° C, stringently washed and red fluorescence representing internalized tau fibrils was quantified by flow cytometry. Bar graph shows normalized fluorescence intensities and standard deviation of n=3 technical replicates. (**C**) CHMP6 knockdown accelerates prion-like propagation of tau aggregation. Representative fluorescence micrographs of the Tau.K18(LM)Clover2 reporter in cells 1 and 2 days after fibril addition. Nuclei were counter-stained with Hoechst 33342. Scale bar = 50 μm (**D**) Quantification of **Fig. 3C**. Tau aggregates were quantified by integrated density across the entire image and divided by total nuclei per image. Error bars represent standard deviation where n=3 images per condition (with at least 50 nuclei per image). *P<0.05, **P<0.01, ***P<0.001 (two-tailed Student's t test for comparison to the values for non-targeting control sgRNA of the same day).

We next sought to evaluate whether knockdown of CHMP6 and VPS13D increased the rate of tau aggregation, or decreased the rate of tau aggregate clearance. To this end, we utilized high-content imaging analysis to track the fibril-induced aggregation of tau over time. As expected from the results in our primary screen, we observed increased levels of aggregates 48 hours post seeding with fibrils when either CHMP6 or VPS13D were knocked down (**Fig. 3C,D**). Intriguingly, the timeline of tau aggregate formation was differentially affected by the two gene knockdowns. While VPS13D knockdown did not cause a statistically significant increase in aggregates 24 hours after treatment with tau fibrils compared to a non-targeting

271     control sgRNA, CHMP6 knockdown promoted early aggregation 24 hours post seeding (**Fig.**

272     **3C,D**). Interestingly, aggregate formation from 24 to 48 hours post-seeding did not change

273     substantially with CHMP6 knockdown, suggesting that the majority of soluble tau rapidly

274     aggregates following treatment with tau fibrils in that background. Given the intriguing

275     acceleration of tau aggregation by CHMP6, and the comparatively weaker phenotype of

276     VPS13D, we decided to focus our mechanistic studies on CHMP6.

277

278     **Endolysosomal escape of tau seeds is rate limiting for propagation of tau aggregation**

279     To investigate the mechanism by which CHMP6 knockdown accelerates seeded tau aggregation,

280     we monitored fibril entry and aggregate formation simultaneously by longitudinal imaging in

281     cells with CHMP6 knockdown compared to cells expressing a non-targeting control sgRNA.

282     (**Fig. 4A**, **Supplementary Movie 1** and **2**). In CHMP6 knockdown cells, large tau aggregates

283     rapidly formed soon after tau fibrils localized to cells, within 12 hours post seeding. In control

284     cells, by contrast, tau fibrils localized to control cells long before aggregates form. We confirmed

285     that these fibril puncta partially colocalize with the late-endosome/lysosome markers RAB7A

286     and LAMP1, and frequently localize to the lumen of RAB7A/LAMP1 positive compartments

287     (**Fig 4B, Supplementary Movie 3** and **4).** These results suggest that fibrils normally accumulate

288     in endolysosomal compartments, where they do not encounter cytosolic tau. However, CHMP6

289     knockdown seems to accelerate exit of fibrils from the endolysosomal pathway into the cytosol,

290     where it can then seed aggregation of cytosolic tau.

291         A mechanism underlying this CHMP6 phenotype is suggested by the recently reported

292     role of the ESCRT machinery in the repair of endolysosomal membrane damage (Skowyra et al.,

293     2018). We hypothesized that knocking down CHMP6 may compromise ESCRT-mediated

294     membrane repair and facilitate tau fibril escape from damaged endolysosomes. We tested this

295     hypothesis by monitoring the formation endolysosomal damage using a cytosolic GFP fusion of

296     galectin 3 (GAL3), a lectin that binds β-galactosides and forms puncta when these sugars are

297     exposed on damaged endolysosomes (Aits et al., 2015). Knocking down CHMP6 indeed caused

298     GAL3-GFP puncta, revealing endolysosomal damage (**Fig. 4C,D**). This demonstrates that

299     CHMP6 plays a critical role in the maintenance of endolysosomal integrity.

300
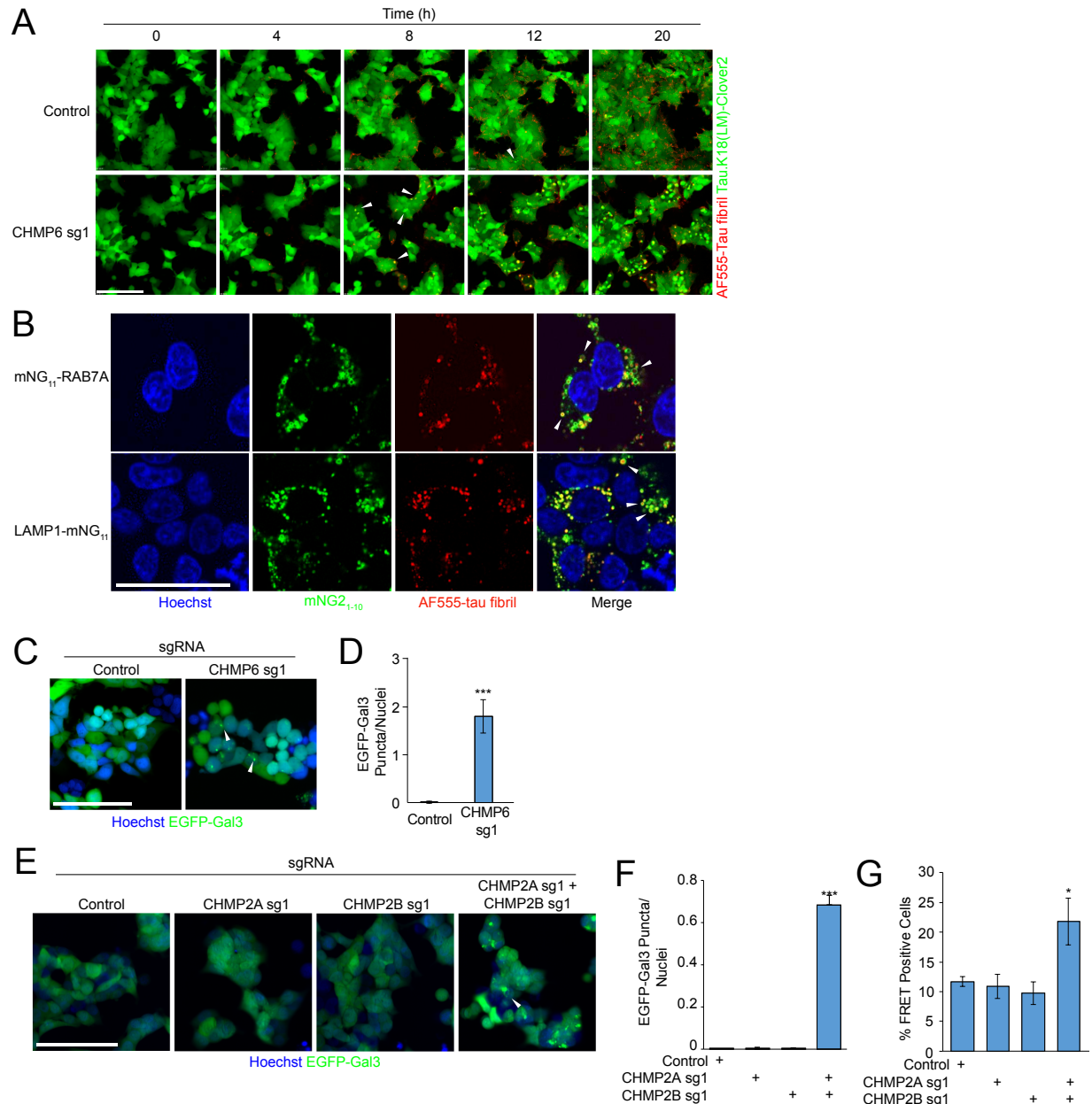
**Figure 4 – CHMP6 knockdown compromises endolysosomal membrane integrity**
(**A**) Time-lapse microscopy of cell entry of tau-AF555 fibrils and resulting aggregation of the cytosolic tau-Clover2 construct. Representative images of CRISPRi-HEK293T cells expressing tau.K18(LM)-clover2 transduced with either non-targeting control (top) or *CHMP6*-targeting sgRNA (bottom) are shown. Scale bar = 50 μm. Corresponding movies are provided as Supplementary Movies 1 (control sgRNA) and 2 (CHMP6 sgRNA). (**B**) Representative fluorescence microscopy images of HEK293T cells with RAB7A or LAMP1 markers endogenously labeled with the split-mNeonGreen system treated with AF555-tau fibrils for 22 hours. AF555-tau fibrils form puncta that partially co-localize with RAB7A and LAMP1-marked endocytic compartments, and in some cases localize to the inner lumen of RAB7A and LAMP1-positive compartments (white arrowheads). Scale bar = 50 μm. Corresponding movies are provided as Supplementary Movies 3 (mNG11-RAB7A) or 4 (LAMP1-mNG11) (**C**) CHMP6 knockdown causes endolysosomal vesicle damage. Representative fluorescence microscopy images of CRISPRi-HEK293T cells expressing an EGFP-Galectin3 (EGFP-Gal3) reporter transduced with either control (*left*)

12

315    or CHMP6 (*right*) sgRNA. Nuclei were counter-stained with Hoechst 33342. (**D**) Quantification of
316    EGFP-Gal3 puncta divided by number of nuclei in fluorescence microscopy images shown in **Fig 4C**.
317    Error bars represent standard deviation for n=3 technical replicates (with at least 50 nuclei per image).
318    ***P<0.001 (two-tailed Student's t test for comparison to the non-targeting control sgRNA). (**E**)
319    Simultaneous, but not individual, knockdown of CHMP2A and CHMP2B results in endolysosomal
320    damage, monitored as in Fig. 4C. Nuclei were counter-stained with Hoechst 33342. Scale bar = 50 μm (**F**)
321    Quantification of EGFP-Gal3 puncta divided by nuclei in fluorescence microscopy images shown in **Fig**
322    **4E**. Error bars represent standard deviation for n=3 technical replicates (with at least 50 nuclei per
323    image). ***P<0.001 (two-tailed Student's t test for comparison to the non-targeting control sgRNA). (**G**)
324    Simultaneous, but not individual, knockdown of CHMP2A and CHMP2B increases prion-like tau
325    aggregation. % FRET positive reporter cells transduced with sgRNAs as indicated 2 days after tau fibril
326    treatment. Error bars represent standard deviation where n=3 technical replicates. *P<0.05 (two-tailed
327    Student's t test for comparison to the non-targeting control sgRNA).

328

329          CHMP6 was the only ESCRT protein that was a strong hit in our primary CRISPRi

330    screen. However, other ESCRT proteins have several paralogues in the human genome, so we

331    hypothesized that these paralogues may have been false-negatives in the CRISPRi screen

332    because they have partially redundant functions. To test this hypothesis, we targeted CHMP2B, a

333    gene with disease-associated mutations involved in familial frontotemporal lobar dementia

334    (FTD). We hypothesized that its phenotype might have been masked by its close homolog,

335    CHMP2A, which could partially compensate for a loss in CHMP2B function. Indeed, we found

336    that simultaneous, but not individual, knockdown of CHMP2A and CHMP2B generated GAL3

337    puncta indicative of endolysosomal damage (**Fig. 4E,F**) and likewise promoted prion-like

338    propagation of tau aggregation (**Fig. 4G**). This finding supports our hypothesis that maintenance

339    of endolysosomal membrane integrity by the broader ESCRT-machinery counteracts

340    endolysosomal escape of tau seeds.

341          A key implication of this model is that endolysosomal damage may promote the prion-

342    like propagation of tau aggregation. To test this concept, we treated cells with Leucyl-Leucyl-o-

343    Methyl-ester (LLOME), a lysosomotropic compound that accumulates in acidified organelles

344    and rapidly forms membranolytic polymers after cleavage by cathepsin C (Thiele & Lipsky,

345    1990; Maejima et al., 2013; Skowyra et al., 2018). We confirmed that LLOME damages

346    endolysosomal membranes in our cell line using the GAL3-GFP reporter (**Fig. 5A,B**).

347    Interestingly, LLOME phenocopied CHMP6 knockdown in its acceleration of seeded tau

348    aggregation only at concentrations where we observe endolysosomal membrane damage (**Fig.**

349    **5C**).

350
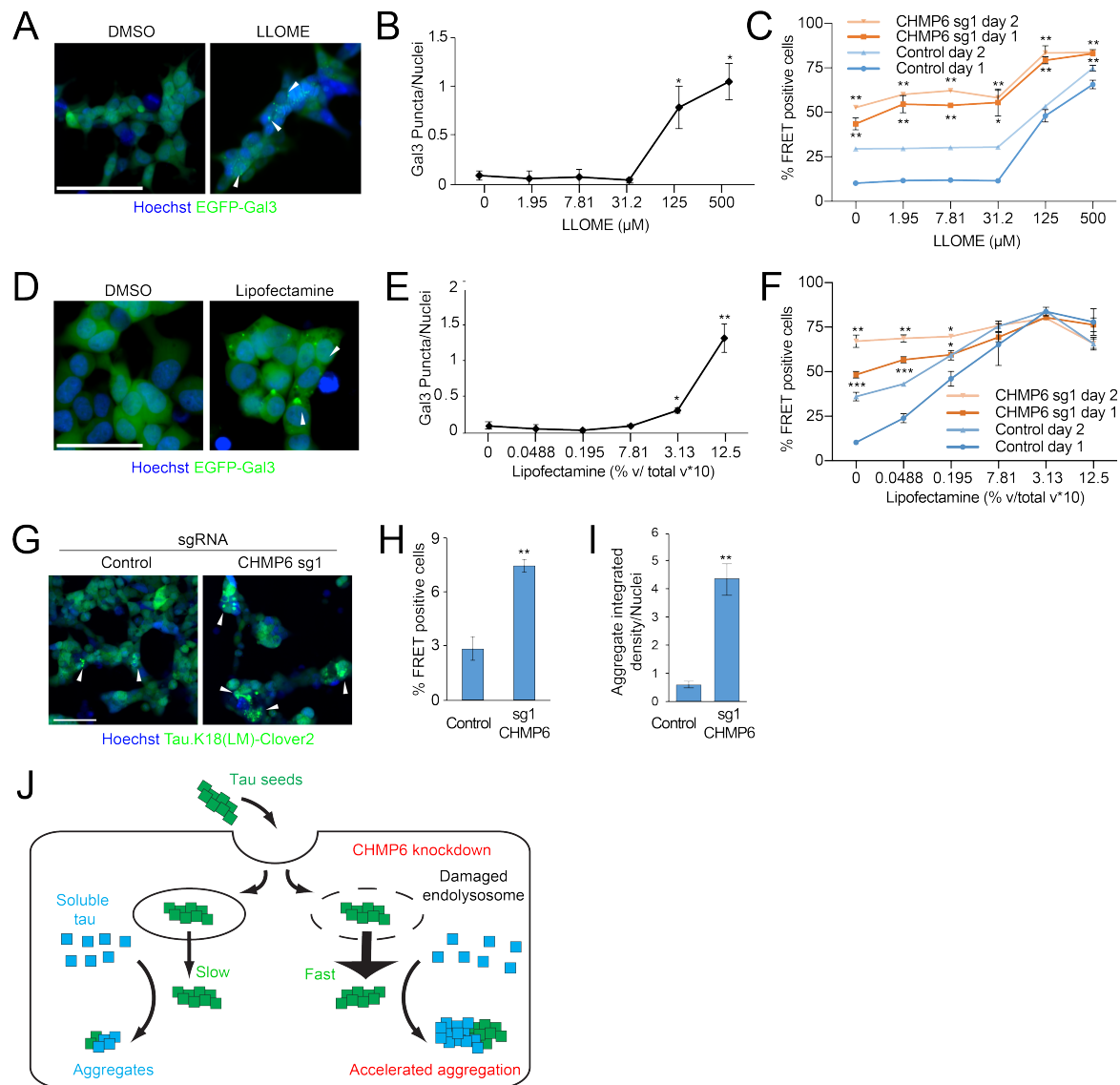
**Figure 5 – Small molecules damage endolysosomal compartments and phenocopy the acceleration of the prion-like propagation of tau aggregation following CHMP6 knockdown**

(**A**) Treatment with the lysosomotropic drug leucyl-leucyl-O-methyl-ester (LLOME) damages endolysosomal vesicles. Representative fluorescence microscopy images of CRISPRi-HEK293T cells expressing the EGFP-Gal3 reporter treated with DMSO (left) or 500 µM LLOME (right) for 24 h. Scale bar = 50 µm (**B**) Quantification of EGFP-Gal3 puncta divided by number of nuclei in fluorescence microscopy images shown in **Fig 5A**. Error bars represent standard deviation for n=3 technical replicates (with at least 50 nuclei per image). ***P<0.001 (two-tailed Student's t test for comparison to DMSO control). (**C**) LLOME treatment accelerates the prion-like propagation of tau aggregation. % FRET positive cells transduced with control (*blue*) or CHMP6 sgRNA (*orange*) were analyzed 24 (*dark line*) or 48 (*light line)* hours following co-treatment with DMSO or increasing concentrations of LLOME and tau fibrils. Error bars represent standard deviation for n=3 technical replicates. *P<0.05, **P<0.01 (two-tailed Student's t test for comparison to the values for non-targeting control sgRNA of the same day) (**D**) Lipofectamine treatment damages endolysosomal vesicles. Representative fluorescence microscopy images of CRISPRi-HEK293T cells expressing the EGFP-Gal3 reporter treated with DMSO (left) or 1.25 % v/v Lipofectamine 2000 (right) for 6 h. Scale bar = 50 µm (**E**) Quantification of EGFP-Gal3 puncta divided by number of nuclei in fluorescence microscopy images shown in **Fig 5D**. Error bars represent

14

369    standard deviation for n=3 technical replicates. ***P<0.001 (two-tailed Student's t test for comparison to
370    no lipofectamine treatment). (**F**) Lipofectamine treatment accelerates the prion-like propagation of tau
371    aggregation. % FRET positive cells transduced with control (*blue*) or CHMP6 sgRNA (*orange*) were
372    analyzed 24 (*dark line*) or 48 (*light line*) hours following co-treatment with PBS or increasing
373    concentrations of lipofectamine 2000 and tau fibrils. Error bars represent standard deviation where n=3
374    technical replicates. *P<0.05, **P<0.01, ***P<0.001 (two-tailed Student's t test for comparison to the
375    values for non-targeting control sgRNA of the same day) (**G-I**) CHMP6 knockdown increases the prion-
376    like propagation tau aggregation when seeding with Alzheimer's patient brain extracts. (G)
377    Representative images of FRET reporter cells transduced with control (*left*) or CHMP6 sgRNA (*right*)
378    and treated with Alzheimer's patient brain extract after 5 days (H) Quantification of images in **Fig. 5G**.
379    Tau aggregates were quantified by integrated density across the entire image and divided by total nuclei
380    per image. Error bars represent standard deviation for n=3 images per condition (with at least 50 nuclei
381    per image). **P<0.01 (two-tailed Student's t test for comparison to non-targeting control sgRNA) (I) %
382    FRET positive cells 5 days following treatment with Alzheimer's patient brain extract. Error bars
383    represent standard deviation where n=3 technical replicates. **P<0.01 (two-tailed Student's t test for
384    comparison to non-targeting control sgRNA). (**J**) Model.
385
386

387         As mentioned above, lipocationic reagents, such as Lipofectamine, are frequently used to

388    deliver tau aggregates to cells for in vitro studies of prion-like propagation (Nonaka et al., 2010;

389    Holmes et al., 2014; Woerman et al., 2016). Interestingly, these agents have previously been

390    demonstrated to induce endolysosomal damage (Zhou & Huang, 1994). Thus, lipocationic agents

391    might facilitate cargo delivery and escape, in part, by causing endolysosomal membrane damage.

392    Indeed, we found that GAL3 puncta indicative of endolysosomal damage are visible 24 hours

393    after treating cells with Lipofectamine (**Fig. 5D,E)**. Moreover, pre-treatment with lipofectamine

394    6 hours prior to seeding cells with tau fibrils significantly increased the formation of tau

395    aggregates in a concentration-dependent manner, including at concentrations lower than the

396    threshold required to induce a Gal3 reporter response (**Fig. 5F**). This suggests that lipofectamine

397    may assist in the prion-like spread of tau aggregates both by acting as a delivery vehicle and

398    damaging endolysosomal membranes.

399         When we combined CHMP6 knockdown with either LLOME or lipofectamine treatment,

400    we found that the relative impact of CHMP6 knockdown on tau aggregate seeding was

401    diminished in the presence of LLOME (**Fig. 5C**) or lipofectamine (**Fig. 5F**), supporting the idea

402    that CHMP6 knockdown and LLOME/lipofectamine treatment promote propagation of tau

403    aggregation at least partially via the same mechanism.

404         Finally, we wanted to validate the CHMP6 phenotype using tau seeds derived from

405    Alzheimer's patient brain-derived extracts. Indeed, we found that CHMP6 knockdown increased

406    the rate of tau aggregation in our reporter line seeded with patient brain-derived tau by both

407 microscopy (**Fig. 5G,H**) and flow cytometry (**Fig. 5I**). Taken together, our results support

408 endolysosomal escape of tau seeds as a rate-limiting step in our cell-based model of prion-like

409 tau propagation. Propagation can be accelerated by compromising endolysosomal integrity either

410 by directly damaging endolysosomes or by interfering with their repair through the ESCRT

411 machinery (**Fig. 5J**).

412

413

414 **DISCUSSION**

415 Using our CRISPRi-based genetic screening platform in a cell-based model of prion-like

416 propagation of tau aggregation, we found that defects in the ESCRT machinery compromise the

417 integrity of the endolysosomal pathway and thereby promote endolysosomal escape of tau seeds

418 and accelerated propagation of tau aggregation. While our observations were made in a cell-

419 based model, it is intriguing to speculate that they are relevant for propagation of tau aggregation

420 in the context of neurodegenerative diseases. Indeed, endolysosomal changes are among the first

421 cellular symptoms in Alzheimer's Disease (Cataldo et al., 2000), and have been postulated to be

422 a central driver of pathogenesis in many neurodegenerative diseases (Hu et al., 2015; Schreij et

423 al., 2016; Small et al., 2017). Furthermore, several risk genes for neurodegenerative diseases are

424 thought to function in the endolysosomal pathway, including CHMP2B (Skibinski et al., 2005).

425 While the ESCRT-III subunit CHMP6 was a top hit in our genetic screen, CHMP2B

426 knockdown by itself did not have a major impact on endolysosomal integrity and the propagation

427 of tau aggregation. This was likely the case because human cells express CHMP2A, a paralogue

428 of CHMP2B which can mostly compensate for CHMP2B in our cell-based model – combined

429 knockdown of CHMP2A and CHMP2B phenocopied CHMP6 knockdown. CHMP6 does not

430 have a paralogue in mammalian cells and is an essential gene, whereas CHMP2B is non-

431 essential, based on the Cancer dependency map, depmap.org (Tsherniak et al., 2017) , and

432 knockout mouse phenotypes (Bult et al., 2019). This provides a rationale for CHMP6 deficiency

433 not being associated with neurodegenerative diseases – it may not be compatible with life.

434 CHMP2B deficiency can be expected to cause a milder phenotype that is unmasked only later in

435 life.

436 Many mechanisms have been proposed to explain the toxicity of tau aggregates.

437 Intriguingly, tau aggregates can damage membranes in vitro (Ait-Bouziad et al., 2017), and may

16

438   damage the endolysomal pathway in patient neurons. In combination with our findings, such a

439   mechanism of toxicity would predict a "vicious circle" or positive-feedback loop, in which tau

440   aggregates would damage the endolysosomal pathway, thereby promoting their own propagation.

441   They could also promote spreading of other aggregates, compatible with the co-occurrence of

442   different protein pathologies, such as tau and a-synuclein, in many cases of neurodegenerative

443   disease (Yan et al., 2018).

444         In summary, our results further support the concept that therapeutic strategies aimed at

445   maintaining or restoring the function of the endolysosomal pathway or promoting its repair may

446   be promising in neurodegenerative diseases. Future studies will be aimed at understanding

447   mechanisms underlying the VPS13D phenotype, which seems distinct from the endolysosomal

448   escape pathway controlled by CHMP6.

449         While our genetic screen with libraries targeting protein homeostasis factors

450   unexpectedly uncovered the ESCRT machinery in counter-acting endolysosomal escape of tau,

451   we had expected to find molecular chaperones or co-chaperones controlling tau aggregation

452   among the top hits. Results obtained *in vitro* (Voss et al., 2012; Baughman et al., 2018; Kundel et

453   al., 2018; Mok et al., 2018) and *in vivo* (Abisambra et al., 2010) suggest that specific chaperones

454   and co-chaperones can strongly modulate tau aggregation, and are potential therapeutic targets

455   for tauopathies (Young et al., 2018). The fact that knockdown of individual chaperones did not

456   have a major impact on tau aggregation could be due to redundancy in the chaperone network of

457   cells. Future CRISPR activation (CRISPRa) screens have the potential to yield complementary

458   results by over-expressing endogenous genes (Gilbert et al., 2014; Kampmann, 2018) and may

459   reveal relevant chaperones in the cellular context.

460         Finally, future screens in iPSC-derived neurons using our recently developed platform

461   (Tian et al., 2019) may reveal additional, neuron-specific pathways, and also uncover factors that

462   underlie selective vulnerability of specific neuronal subtypes (Kampmann, 2017).

463

464

465

**MATERIALS AND METHODS**

**Preparation of extracts from Alzheimer's Disease patient brains**

The Alzheimer's Disease brain sample was received from the Neurodegenerative Brain Bank of the UCSF Memory and Aging Center (UCSF/MAC) . All research participants at UCSF/MAC undergo longitudinal clinical and imaging assessment. Upon death, the fresh brain was slabbed into 8- to 10-mm thick coronal slabs upon procurement. These slabs were alternately fixed, in 10% neutral buffered formalin for 72 hours, or snap frozen. Twenty-six tissue blocks covering dementia-related regions of interest were dissected from the fixed slabs, and hematoxylin and eosin and immunohistochemical stains were applied following standard diagnostic procedures developed for patients with dementia (Hyman & Trojanowski, 1997; Tartaglia et al., 2010). Immunohistochemistry was performed using antibodies against TDP-43 (rabbit, 1:2000, Proteintech Group, Chicago, IL, USA), hyperphosphorylated tau (CP-13, S202/T205, mouse, 1:250, courtesy of P. Davies), beta-amyloid (1-16, mouse, clone DE2, 1:500, Millipore, Billerica, MA, USA), alpha-synuclein (LB509, mouse, 1:5000, courtesy of J. Trojanowski and V. Lee). All immunohistochemical runs included positive control sections to exclude technical factors as a cause of absent immunoreactivity. Neuropathological diagnosis followed currently accepted guidelines (Hauw et al., 1994; Dickson et al., 2002; McKeith et al., 2005; Cairns et al., 2007; Montine et al., 2012). For this study, a region from the parietal cortex containing high amount of AD-tau pathology was sampled from a snap frozen block. A brain extract was prepared and phosphotungstate-insoluble fractions were purified as previously described (Woerman et al., 2016). The extract was diluted in PBS 1:40 in DPBS and flash frozen in liquid nitrogen and stored at -80 ºC.

**Purification, characterization, labeling, and fibrillization of recombinant tau**

Human WT 0N4R-6xHis tau protein was expressed in Rosetta$^{TM}$ 2(DE3) competent cells (MilliporeSigma #71400-3) essentially as previously described (Mok et al., 2018). Briefly, protein expression was induced with 200 μM IPTG for 3.5 hours at 30 ºC. Cells were lysed via a microfluidizer (Microfluidics Cat# M-100EH) followed by boiling of the lysate for 20 min. The clarified supernatant was subsequently dialyzed overnight into Buffer A (20 mM MES pH 6.8, 50 mM NaCl, 1mM EGTA, 1 mM MgCl2, 2 mM DTT, 0.1 mM PMSF) and purified by cation

18

497  exchange using a HiTrap Capto SP ImpRes column (GE Cat# 17546851) with elution buffer

498  (Buffer A with 1 M NaCl). Fractions containing tau as determined by Coomassie-stained SDS-

499  PAGE were dialyzed into PBS, concentrated with an Amicon Ultra-15 centrifugal 3 kDa MWCO

500  filter (Millipore Cat# UFC900324), endotoxin purified using a Pierce high capacity endotoxin

501  removal spin column (ThermoFisher Cat# 88274), filter sterilized using a Millex-GV syringe

502  filter unit (Millipore Cat# SLGV033RB), and snap frozen in PBS at -80 ºC. Aggregation was

503  induced by incubating 10 μM tau (0.43 mg/mL) with .022 mg/mL heparin (Fisher Cat# 9041-08-

504  1, lot# 177772) and shaken at 37 °C overnight in a shaker at 1200 rpm (VWR Cat#12620-942).

505  To generate fluorescently labeled tau fibrils, 0.6 μl 10 mg/mL Alexa Fluor-555

506  (ThermoFisher Cat# A37571), 180 μl of 0.43 mg/mL tau fibrils, and 19.4 μl 1M sodium

507  bicarbonate were mixed at room temperature in the dark for 1h. Labeled tau fibrils were

508  subsequently purified from unlabeled dye with using a Zeba 7k MWCO spin desalting column

509  (ThermoFisher Cat# 89882).

510  Tau fibrils were negatively stained with 0.75% uranyl formate (pH 5.5-6.0) on thin

511  amorphous carbon layered 400-mesh copper grids (Pelco Cat# 1GC400). Five μL of sample was

512  applied to the grid for 20s before taking the droplet off with Whatman paper, followed by two

513  washes with 5 μL ddH2O and three applications of 5 μL uranyl formate removed by vacuum.

514  Grids were imaged at room temperature using a Fei Tecnai 12 microscope operating at 120kV.

515  Images were acquired on a US 4000 CCD camera at 66873x resulting in a sampling of 2.21

516  Angstrom/pixel.

517

518  **Plasmid and library design and construction**

519  Plasmids for the FRET-based aggregation reporter were constructed by cloning a fusion of the

520  K18 repeat domain of tau containing the P301L/V337M mutation (Kfoury et al., 2012) in frame

521  with C-terminal Clover2 (Addgene #54711) or mRuby2 (Addgene #54768, (Lam et al., 2012),

522  gifts from Michael Davidson, into the lentiviral expression vector pMK1200 (Kampmann et al.,

523  2013), Addgene #84219) under the control of the constitutive EF1A promoter, to obtain

524  pMK1253 or pMK1254, respectively.

525  Pooled CRISPRi sgRNA libraries targeting human protein homeostasis genes were

526  designed using our next-generation algorithm (Horlbeck et al., 2016). SgRNA protospacers for

527  these libraries are listed in Table S2. Oligonucleotide pools encoding the library were

19

528    synthesized by Agilent, PCR amplified and cloned into our optimized lentiviral sgRNA

529    expression vector as previously described (Gilbert et al., 2014).

530        For generation of individual sgRNAs, pairs of oligonucleotides (IDT) were annealed and

531    ligated into our optimized lentiviral sgRNA expression vector. For double sgRNA expression

532    constructs, CHMP2B and CHMP2A targeting oligos were annealed and ligated into pMJ114 and

533    pMJ179, and a double-sgRNA vector was generated from these as previously described

534    (Adamson et al., 2016).

535        The fluorescent Gal3 reporter was PCR amplified from pEGFP-hGal3 (Addgene

536    #73080), a gift from Tamotsu Yoshimori) and Gibson cloned into pJC41, which uses the

537    pMK1200 backbone (described above) and replaces the EF1a promoter with a CAG promoter.

538

**Cell culture, cell line generation, and treatment conditions**

540    All cells were maintained in a tissue culture incubator (37 °C, 5% $CO_2$) and checked regularly for

541    mycoplasma contamination. HEK293T cells were cultured in DMEM supplemented with 10%

542    fetal bovine serum (Seradigm Cat# 97068-085, Lot# 076B16), Pen/Strep (Life Cat# 15140122),

543    and L-glutamine (Life Cat# 25030081).

544        To generate the FRET reporter line, HEK293T cells were infected with lentivirus from

545    plasmids pMK1253 and pMK1254 and cells with the highest dynamic FRET signal 2 days after

546    seeding with tau fibrils were selected. To introduce CRISPRi functionality, the cells were

547    lentivirally transduced with pHR-SFFV-dCas9-BFP-KRAB (Addgene # 46911, a gift from

548    Stanley Qi & Jonathan Weissman (Gilbert et al., 2013)), mono-clonal cell lines were selected

549    and CRISPRi activity was validated as previously described (Tian et al., 2019).

550        Cellular markers were endogenously labeled using the split-mNeonGreen2 system (Feng

551    et al., 2017), following conditions described in (Leonetti et al., 2016). Briefly, synthetic guide

552    RNAs (IDT, Alt-R reagents) were first complexed in vitro with purified *S. Pyogenes* Cas9

553    protein (UC Berkeley Macrolab). Cas9/RNA complexes were then mixed with single-stranded

554    DNA oligo donors (IDT, Ultramer reagents) and nucleofected (Lonza Cat#AAF-1002B, Amaxa

555    program CM-130) into HEK cells stably expressing SFFV-mNeonGreen2$_{1-10}$. Fluorescent cells

556    were selected by flow cytometry (SONY biotechnology Cat# SH800S). Sequences for CRISPR

557    RNA and donors used are listed as follows:

558

| Target | crRNA sequence | Donor oligonucleotide sequence |
|---|---|---|
| LAMP1 (C-term mNG11) | 5'-GTGCACCAGGCTAGATAGTC -3' | 5'-CCCAGAGAAAGGAACAGAGGCCCCTGCAGCTGCTGTGCCTGCGTGCACCAGGCTACATCATATCGGTAAAGGCCTTTTGCCACTCCTTGAAGTTGAGCTCGGTACCACTTCCTGGACCTTGAAACAAAACTTCCAATCCGCCACCGATAGTCTGGTAGCCTGCGTGACTCCTCTTCCTGCCGACGAGGTAGGCGATGAGG -3' |
| RAB7A (N-term mNG11) | 5'-TAGTTTGAAGGATGACCTCT -3' | 5'-TGTTTCCATCACACTCACAGTGATTTCTCCTTTTCCCCCTTTAGTTTGAAGGATGACCGAGCTCAACTTCAAGGAGTGGCAAAAGGCCTTTACCGATATGATGGGTGGCGGATTGGAAGTTTTGTTTCAAGGTCCAGGAAGTGGTACCTCTAGGAAGAAAGTGTTGCTGAAGGTTATCATCCTGGGAGATTCTGGGTAAG -3' |

559

560  To generate CRISPRi-HEK293T cells that monitor EGFP-Gal3 damage or only generate

561 tau.K18(LM)-Clover2 aggregates, CRISPRi-HEK293T cells were lentivirally transduced with

562 pMK1253 and pJC41, and a polyclonal population was sorted by FACS.

563

564 **Primary CRISPRi screen**

565 For pooled screening of libraries, 7.5 million HEK293T cells were seeded into a 15 cm$^2$ plate

566 with complete DMEM on day 0. On day 1, 5 μg of lentiviral plasmid packaging mix (Kampmann

567 et al., 2014) and 5 μg of pooled sgRNA library plasmid was transfected using lipofectamine

568 2000 (ThermoFisher Cat# 11668019) and incubated for 2 days. On day 3, conditioned media was

569 removed and filter sterilized using a Millex-GV syringe filter unit (Millipore Cat#

570 SLGV033RB). Lentivirus was precipitated (Alstem Cat# VC100) according to manufacturer

21

571  protocols and resuspended in complete DMEM. 20 million FRET reporter cells were added to

572  lentivirus-containing media and seeded into a T175 flask. On day 4, media from the T175 was

573  replaced with DMEM complete with 2.5 μg/mL puromycin. On day 8, Cells infected with pooled

574  sgRNA libraries were trypsinized and replated into at 100 μl per well (25,000 cells/well) of

575  several 96-well plate. In addition, 0.3 μl of 0.43 μg/μL of tau fibrils were added to each well. 48

576  hours later, cells were trypsinized and sorted using an Aria II FACS cytometer into FRET

577  negative and FRET positive populations. Genomic DNA was isolated using a Macherey-Nagel

578  Blood L kit (Machery-Nagel Cat# 740954.20) and followed according to manufacturer protocols.

579  SgRNA-encoding regions were then amplified and sequenced as previously published (Gilbert et

580  al., 2014). Phenotypes and P values for each gene were calculated using our most recent

581  bioinformatics pipeline (https://kampmannlab.ucsf.edu/mageck-inc (Tian et al., 2019)). For

582  genes targeted by more than one sgRNA library, values for the more significant phenotype were

583  selected. Full results are listed in Table S1.

584

585  **Secondary assays based on microscopy and flow cytometry**

586  To monitor tau aggregation, FRET reporter cells were seeded (25,000 cells/well) into 100 μL per

587  well in a 96 well black bottom plates (Greiner Bio-One #655097) with 0.3 μL 0.43 mg/mL Tau

588  fibrils on day 1 and analyzed 24 or 48 hours after seeding. For Alzheimer's patient brain extracts,

589  1.5 μL extract, 0.375% total v/v Lipofectamine 2000 (ThermoFisher Cat# 11668019), and 7.85

590  μL OptiMEM (Thermo Cat# 31985062) were mixed and incubated at room temperature for 2

591  hours. Lipofectamine-brain extract complexes were then added to cells previously plated in 100

592  μL (10,000 cells/well) for 6 hours. Cells were analyzed 5 days after seeding. For analysis, cells

593  were stained with Hoechst 33342 (ThermoFisher Cat# 5553141) at 1 μg/mL and analyzed by

594  flow cytometry using a BD FACSCelesta or by fluorescence microscopy using an InCell 6000

595  (GE Cat# 28-9938-51). Digital images were analyzed using CellProfiler by counting the

596  integrated density of identified aggregates/nuclei and averaged between 3 images. Cells with

597  sgRNA knockdown were similarly analyzed using a comparable protocol 5 days after

598  transduction with individual sgRNA-encoding lentivirus.

599        For experiments measuring tau aggregation in the presence of inducers of endolysosmal

600  damage, FRET reporter cells were seeded (25,000 cells/well) into 100 μL per well in a 96 well

601  black bottom plate and treated with LLOME (Sigma Cat# L7393-500MG) at varying

22

602    concentrations with 0.3 μL 0.43 μg/μL Tau fibrils. For treatment with lipofectamine 2000, FRET

603    reporter cells were seeded (25,000 cells/well) into 100 μL per well in a 96 well black bottom

604    plate and treated with Lipofectamine 2000 at varying concentrations. Cells were then treated 0.3

605    μL 0.43 μg/μL Tau fibrils 6 hours later. 24 or 48 hours later after seeding, cells were stained with

606    Hoechst 33342 (1 μg/mL) and analyzed by flow cytometry using a BD FACSCelesta or by

607    fluorescence microscopy using an InCell 6000 GE (Cat# 28-9938-51). Digital images were

608    collected and analyzed using CellProfiler by quantifying the integrated density of identified

609    aggregates and Hoechst-stained nuclei. In cases where CellProfiler was unable to identify nuclei,

610    nuclei were counted interactively using ImageJ. Cells with sgRNA knockdown were similarly

611    analyzed using a comparable protocol 5 days after transduction with individual sgRNA-encoding

612    lentivirus.

613        To monitor tau fibril uptake, on day 0, CRISPRi-HEK293T cells previously transduced

614    for 5 days with lentivirus expressing single sgRNAs were seeded (25,000 cells/well) into 100 μL

615    per well in a 96-well plate. On day 1, cells were treated with 1 μL 0.39 μg/μL AF555-tau fibril

616    for 1 hr at 37 ºC and collected for analysis by flow cytometry. Median mRuby2 values were

617    calculated in FlowJo and averaged between 3 technical replicates.

618        To monitor tau.K18(LM)-Clover2 steady-state levels, on day 0, FRET reporter cells

619    previously transduced for 5 days with lentivirus expressing single sgRNAs were seeded (25,000

620    cells/well) into 100 μL per well in a 96-well plate. On day 1, cells collected for analysis by flow

621    cytometry. Median Clover2 values were calculated in FlowJo and averaged between 3 technical

622    replicates.

623        To monitor localization of AF555-labeled tau fibrils, HEK293T cells expressing

624    Tau.K18(LM)-Clover2 were seeded (12,500 cells/well) into 100 μL per well in a 96-well black

625    bottom plate (Greiner Bio-One #655097) on day 0 in complete DMEM. On day 1, 0.3 μL 0.39

626    μg/μL AF555-tau fibrils were added to cell culture media and placed into an InCell 6000 (GE

627    Cat# 28-9938-51) incubator. Images were taken by at 20 minute intervals between incubations.

628        To monitor co-localization of tau fibrils with RAB7A and LAMP1, fluorescently labeled

629    HEK293T cells were seeded in glass-bottom 96-well plates (Cellvis #P96-1.5P) pre-coated with

630    fibronectin (Roche Cat# 11051407001) at 25,000 cells cells/well in 150 μL complete DMEM

631    media (including 10% FBS). After incubation for 3 hours to allow for cell adhesion, cells were

632    treated with 0.11 μg of AF555-tau PFFs per well. 22 hours post-treatment, cells were counter-

23

633    stained with Hoechst 33342 (0.5 µg/mL, 30 min at 37 ºC) and imaged in complete DMEM

634    without phenol-red. Live-cell imaging was performed on a Dragonfly spinning-disk instrument

635    (Andor) at 37 ºC in 5% CO2 atmosphere equipped with a 63x/1.47 NA objective (Leica) and an

636    iXon Ultra 888 EMCCD camera (Andor), acquiring time-lapse datasets at 0.4Hz.

637         To monitor Gal3-EGFP puncta formation, CRISPRi-HEK293T cells expressing EGFP-

638    Gal3 were seeded into 100 µL per well (25,000 cells/well) in a 96 well black bottom plates and

639    treated with LLOME or Lipofectamine at varying concentrations. 24 hours after seeding, cells

640    were stained with Hoechst 33342 (1 µg/mL) and digital images were collected and analyzed by

641    an InCell 6000 by counting EGFP-Gal3 puncta/nuclei and averaged between 3 images. Cells

642    with sgRNA knockdown were similarly analyzed using a comparable protocol 5 days after

643    transduction with individual sgRNA-encoding lentivirus and puromycin selection of transduced

644    cells.

645

646    **Cell fractionation and immunoblot**

647    Cells were seeded into 3 mL at 250,000 cells/well in a 6-well dishes with 4.8 µl 0.43 mg/mL tau

648    fibrils, and harvested after 48 hours by washing with PBS and releasing with 0.25% trypsin.

649    Cells were resuspended with DMEM pre-warmed to 37 ºC, spun down and washed again with

650    PBS. Cells were resuspended in 20 µl PBS and lysed by flash freezing on dry ice and rapidly

651    thawed at 42 C. This step was repeated twice. The resulting lysate was spun at 1000xg and the

652    resulting supernatant was transferred to a new tube and respun to remove any carry-over

653    insoluble material.  The pellet was rinsed 3x with PBS and resuspended to the corresponding

654    volume of supernatant and briefly sonicated with a tip sonicator (Sonopuls 2070) for a brief 1

655    second pulse at 10% maximum intensity. Equivalent fractions of total volume for 100 ng

656    supernatant and resuspended pellet were boiled with SDS loading buffer (50 mM Tris-Cl

657    (pH6.8), 2% (2 w/v) SDS, 0.1% (w/v) bromophenol blue) and 10 mM DTT, subjected to SDS-

658    PAGE on 4-12% Bis-Tris polyacrylamide gels (ThermoFisher Cat# NP0322BOX) and

659    transferred to nitrocellulose membranes. Primary antibodies against human tau (DAKO Cat#

660    A0024) and β-actin (Cell Signaling Cat# 3700) were used to detect proteins. Blots were then

661    incubated with secondary antibodies (Li-Cor Cat# 926-32213 and 926-68072) and imaged on the

662    Odyssey Fc Imaging system (Li-Cor Cat# 2800). Digital images were processed and analyzed

663    using Licor Image Studio$^{TM}$ software.

664

**qRT-PCR**

CRISPRi-HEK293T cells expressing a constitutive non-targeting or targeting sgRNA were collected by centrifugation at 1000xg for 10 min, washed twice with ice cold PBS and processed for qPCR using a RNA purification kit (Zymo Cat# D7011). 500 ng total RNA from each sample were reverse transcribed using Superscript$^{TM}$ III reverse transcriptase using an oligo(dT) primer (Invitrogen Cat# 18080044). The resulting cDNA was diluted 5-fold using 10 mM Tris pH 8.0 and 0.67 μL of this dilution was used for each quantitative real-time PCR (qPCR) reaction. qPCR reactions were set up using SensiMix 2x Mastermix (Bioline Cat# QT615-20) and oligonucleotides targeting genes of interest (IDT) in triplicate and run on QuantStudio 6 Flex (Applied Biosystems Cat# 4485694) using protocols according to the mastermix manufacturer's specifications. All reactions were normalized to an internal loading control (GAPDH) and the sgRNA activity is expressed as knockdown efficiency. The qPCR primer sequences are listed in Table S2.

**AUTHOR CONTRIBUTIONS**

Conception and design: J.C.C., M.K.

Acquisition of data: J.C.C., D.T.N., P.R., M.N., E.T.

Analysis and interpretation of data: J.C.C., D.L.N., M.N., R.T., E.T., P.R., M.L., D.S., M.K.

Drafting or revising the article: J.C.C., M.K.

Contributing unpublished essential data or reagents: J.Y.H., S.K.S., S.M., L.T.G., J.E.G.

706

707

## REFERENCES

709

710   Abisambra, J. F., Blair, L. J., Hill, S. E., Jones, J. R., Kraft, C., Rogers, J., Koren, J., 3rd, Jinwal,
711         U. K., Lawson, L., Johnson, A. G., Wilcock, D., O'Leary, J. C., Jansen-West, K.,
712         Muschol, M., Golde, T. E., Weeber, E. J., Banko, J., & Dickey, C. A. (2010).
713         Phosphorylation dynamics regulate Hsp27-mediated rescue of neuronal plasticity deficits
714         in tau transgenic mice. *J Neurosci, 30*(46), 15374-15382.
715         doi:10.1523/JNEUROSCI.3155-10.2010

716   Adamson, B., Norman, T. M., Jost, M., Cho, M. Y., Nunez, J. K., Chen, Y., Villalta, J. E.,
717         Gilbert, L. A., Horlbeck, M. A., Hein, M. Y., Pak, R. A., Gray, A. N., Gross, C. A., Dixit,
718         A., Parnas, O., Regev, A., & Weissman, J. S. (2016). A Multiplexed Single-Cell CRISPR
719         Screening Platform Enables Systematic Dissection of the Unfolded Protein Response.
720         *Cell, 167*(7), 1867-1882 e1821. doi:10.1016/j.cell.2016.11.048

721   Ait-Bouziad, N., Lv, G., Mahul-Mellier, A. L., Xiao, S., Zorludemir, G., Eliezer, D., Walz, T., &
722         Lashuel, H. A. (2017). Discovery and characterization of stable and toxic
723         Tau/phospholipid oligomeric complexes. *Nat Commun, 8*(1), 1678. doi:10.1038/s41467-
724         017-01575-4

725   Aits, S., Kricker, J., Liu, B., Ellegaard, A. M., Hamalisto, S., Tvingsholm, S., Corcelle-Termeau,
726         E., Hogh, S., Farkas, T., Holm Jonassen, A., Gromova, I., Mortensen, M., & Jaattela, M.
727         (2015). Sensitive detection of lysosomal membrane permeabilization by lysosomal
728         galectin puncta assay. *Autophagy, 11*(8), 1408-1424.
729         doi:10.1080/15548627.2015.1063871

730   Baughman, H. E. R., Clouser, A. F., Klevit, R. E., & Nath, A. (2018). HspB1 and Hsc70
731        chaperones engage distinct tau species and have different inhibitory effects on amyloid
732        formation. *J Biol Chem, 293*(8), 2687-2700. doi:10.1074/jbc.M117.803411

733   Bejanin, A., Schonhaut, D. R., La Joie, R., Kramer, J. H., Baker, S. L., Sosa, N., Ayakta, N.,
734        Cantwell, A., Janabi, M., Lauriola, M., O'Neil, J. P., Gorno-Tempini, M. L., Miller, Z. A.,
735        Rosen, H. J., Miller, B. L., Jagust, W. J., & Rabinovici, G. D. (2017). Tau pathology and
736        neurodegeneration contribute to cognitive impairment in Alzheimer's disease. *Brain,*
737        *140*(12), 3286-3300. doi:10.1093/brain/awx243

738   Berg, L., McKeel, D. W., Jr., Miller, J. P., Storandt, M., Rubin, E. H., Morris, J. C., Baty, J.,
739        Coats, M., Norton, J., Goate, A. M., Price, J. L., Gearing, M., Mirra, S. S., & Saunders,
740        A. M. (1998). Clinicopathologic studies in cognitively healthy aging and Alzheimer's
741        disease: relation of histologic markers to dementia severity, age, sex, and apolipoprotein
742        E genotype. *Arch Neurol, 55*(3), 326-335.

743   Bult, C. J., Blake, J. A., Smith, C. L., Kadin, J. A., Richardson, J. E., & Mouse Genome
744        Database, G. (2019). Mouse Genome Database (MGD) 2019. *Nucleic Acids Res, 47*(D1),
745        D801-D806. doi:10.1093/nar/gky1056

746   Cairns, N. J., Bigio, E. H., Mackenzie, I. R., Neumann, M., Lee, V. M., Hatanpaa, K. J., White,
747        C. L., 3rd, Schneider, J. A., Grinberg, L. T., Halliday, G., Duyckaerts, C., Lowe, J. S.,
748        Holm, I. E., Tolnay, M., Okamoto, K., Yokoo, H., Murayama, S., Woulfe, J., Munoz, D.
749        G., Dickson, D. W., Ince, P. G., Trojanowski, J. Q., Mann, D. M., & Consortium for
750        Frontotemporal Lobar, D. (2007). Neuropathologic diagnostic and nosologic criteria for
751        frontotemporal lobar degeneration: consensus of the Consortium for Frontotemporal
752        Lobar Degeneration. *Acta Neuropathol, 114*(1), 5-22. doi:10.1007/s00401-007-0237-2

753   Cataldo, A. M., Peterhoff, C. M., Troncoso, J. C., Gomez-Isla, T., Hyman, B. T., & Nixon, R. A.
754        (2000). Endocytic pathway abnormalities precede amyloid beta deposition in sporadic
755        Alzheimer's disease and Down syndrome: differential effects of APOE genotype and
756        presenilin mutations. *Am J Pathol, 157*(1), 277-286.

757   Clayton, E. L., Mizielinska, S., Edgar, J. R., Nielsen, T. T., Marshall, S., Norona, F. E., Robbins,
758        M., Damirji, H., Holm, I. E., Johannsen, P., Nielsen, J. E., Asante, E. A., Collinge, J.,
759        consortium, F. R., & Isaacs, A. M. (2015). Frontotemporal dementia caused by CHMP2B
760        mutation is characterised by neuronal lysosomal storage pathology. *Acta Neuropathol,*
761        *130*(4), 511-523. doi:10.1007/s00401-015-1475-3

762   Dickson, D. W., Bergeron, C., Chin, S. S., Duyckaerts, C., Horoupian, D., Ikeda, K., Jellinger,
763        K., Lantos, P. L., Lippa, C. F., Mirra, S. S., Tabaton, M., Vonsattel, J. P., Wakabayashi,
764        K., Litvan, I., & Office of Rare Diseases of the National Institutes of, H. (2002). Office of
765        Rare Diseases neuropathologic criteria for corticobasal degeneration. *J Neuropathol Exp*
766        *Neurol, 61*(11), 935-946.

767   Feng, S., Sekine, S., Pessino, V., Li, H., Leonetti, M. D., & Huang, B. (2017). Improved split
768        fluorescent proteins for endogenous protein labeling. *Nat Commun, 8*(1), 370.
769        doi:10.1038/s41467-017-00494-8

770  Frost, B., Jacks, R. L., & Diamond, M. I. (2009). Propagation of tau misfolding from the outside
771       to the inside of a cell. *J Biol Chem, 284*(19), 12845-12852. doi:10.1074/jbc.M808759200

772  Giannakopoulos, P., Herrmann, F. R., Bussiere, T., Bouras, C., Kovari, E., Perl, D. P., Morrison,
773       J. H., Gold, G., & Hof, P. R. (2003). Tangle and neuron numbers, but not amyloid load,
774       predict cognitive status in Alzheimer's disease. *Neurology, 60*(9), 1495-1500.

775  Gilbert, L. A., Horlbeck, M. A., Adamson, B., Villalta, J. E., Chen, Y., Whitehead, E. H.,
776       Guimaraes, C., Panning, B., Ploegh, H. L., Bassik, M. C., Qi, L. S., Kampmann, M., &
777       Weissman, J. S. (2014). Genome-Scale CRISPR-Mediated Control of Gene Repression
778       and Activation. *Cell, 159*(3), 647-661. doi:10.1016/j.cell.2014.09.029

779  Gilbert, L. A., Larson, M. H., Morsut, L., Liu, Z., Brar, G. A., Torres, S. E., Stern-Ginossar, N.,
780       Brandman, O., Whitehead, E. H., Doudna, J. A., Lim, W. A., Weissman, J. S., & Qi, L. S.
781       (2013). CRISPR-mediated modular RNA-guided regulation of transcription in
782       eukaryotes. *Cell, 154*(2), 442-451. doi:10.1016/j.cell.2013.06.044

783  Gomez-Isla, T., Hollister, R., West, H., Mui, S., Growdon, J. H., Petersen, R. C., Parisi, J. E., &
784       Hyman, B. T. (1997). Neuronal loss correlates with but exceeds neurofibrillary tangles in
785       Alzheimer's disease. *Ann Neurol, 41*(1), 17-24. doi:10.1002/ana.410410106

786  Hauw, J. J., Daniel, S. E., Dickson, D., Horoupian, D. S., Jellinger, K., Lantos, P. L., McKee, A.,
787       Tabaton, M., & Litvan, I. (1994). Preliminary NINDS neuropathologic criteria for Steele-
788       Richardson-Olszewski syndrome (progressive supranuclear palsy). *Neurology, 44*(11),
789       2015-2019.

790  Holmes, B. B., DeVos, S. L., Kfoury, N., Li, M., Jacks, R., Yanamandra, K., Ouidja, M. O.,
791       Brodsky, F. M., Marasa, J., Bagchi, D. P., Kotzbauer, P. T., Miller, T. M., Papy-Garcia,
792       D., & Diamond, M. I. (2013). Heparan sulfate proteoglycans mediate internalization and
793       propagation of specific proteopathic seeds. *Proc Natl Acad Sci U S A, 110*(33), E3138-
794       3147. doi:10.1073/pnas.1301440110

795  Holmes, B. B., Furman, J. L., Mahan, T. E., Yamasaki, T. R., Mirbaha, H., Eades, W. C.,
796       Belaygorod, L., Cairns, N. J., Holtzman, D. M., & Diamond, M. I. (2014). Proteopathic
797       tau seeding predicts tauopathy in vivo. *Proc Natl Acad Sci U S A, 111*(41), E4376-4385.
798       doi:10.1073/pnas.1411649111

799  Horlbeck, M. A., Gilbert, L. A., Villalta, J. E., Adamson, B., Pak, R. A., Chen, Y., Fields, A. P.,
800       Park, C. Y., Corn, J. E., Kampmann, M., & Weissman, J. S. (2016). Compact and highly
801       active next-generation libraries for CRISPR-mediated gene repression and activation.
802       *Elife, 5*. doi:10.7554/eLife.19760

803  Hu, Y. B., Dammer, E. B., Ren, R. J., & Wang, G. (2015). The endosomal-lysosomal system:
804       from acidification and cargo sorting to neurodegeneration. *Transl Neurodegener, 4*, 18.
805       doi:10.1186/s40035-015-0041-1

806  Hurley, J. H. (2015). ESCRTs are everywhere. *EMBO J, 34*(19), 2398-2407.
807       doi:10.15252/embj.201592484

808 Hyman, B. T., & Trojanowski, J. Q. (1997). Consensus recommendations for the postmortem
809       diagnosis of Alzheimer disease from the National Institute on Aging and the Reagan
810       Institute Working Group on diagnostic criteria for the neuropathological assessment of
811       Alzheimer disease. *J Neuropathol Exp Neurol, 56*(10), 1095-1097.

812 Kampmann, M. (2017). A CRISPR Approach to Neurodegenerative Diseases. *Trends Mol Med,*
813       *23*(6), 483-485. doi:10.1016/j.molmed.2017.04.003

814 Kampmann, M. (2018). CRISPRi and CRISPRa Screens in Mammalian Cells for Precision
815       Biology and Medicine. *ACS Chem Biol, 13*(2), 406-416.
816       doi:10.1021/acschembio.7b00657

817 Kampmann, M., Bassik, M. C., & Weissman, J. S. (2013). Integrated platform for genome-wide
818       screening and construction of high-density genetic interaction maps in mammalian cells.
819       *Proc Natl Acad Sci U S A, 110*(25), E2317-2326. doi:10.1073/pnas.1307002110

820 Kampmann, M., Bassik, M. C., & Weissman, J. S. (2014). Functional genomics platform for
821       pooled screening and generation of mammalian genetic interaction maps. *Nat Protoc,*
822       *9*(8), 1825-1847. doi:10.1038/nprot.2014.103

823 Kaufman, S. K., Sanders, D. W., Thomas, T. L., Ruchinskas, A. J., Vaquer-Alicea, J., Sharma,
824       A. M., Miller, T. M., & Diamond, M. I. (2016). Tau Prion Strains Dictate Patterns of Cell
825       Pathology, Progression Rate, and Regional Vulnerability In Vivo. *Neuron, 92*(4), 796-
826       812. doi:10.1016/j.neuron.2016.09.055

827 Kfoury, N., Holmes, B. B., Jiang, H., Holtzman, D. M., & Diamond, M. I. (2012). Trans-cellular
828       propagation of Tau aggregation by fibrillar species. *J Biol Chem, 287*(23), 19440-19451.
829       doi:10.1074/jbc.M112.346072

830 Kumar, N., Leonzino, M., Hancock-Cerutti, W., Horenkamp, F. A., Li, P., Lees, J. A., Wheeler,
831       H., Reinisch, K. M., & De Camilli, P. (2018). VPS13A and VPS13C are lipid transport
832       proteins differentially localized at ER contact sites. *J Cell Biol, 217*(10), 3625-3639.
833       doi:10.1083/jcb.201807019

834 Kundel, F., De, S., Flagmeier, P., Horrocks, M. H., Kjaergaard, M., Shammas, S. L., Jackson, S.
835       E., Dobson, C. M., & Klenerman, D. (2018). Hsp70 Inhibits the Nucleation and
836       Elongation of Tau and Sequesters Tau Aggregates with High Affinity. *ACS Chem Biol,*
837       *13*(3), 636-646. doi:10.1021/acschembio.7b01039

838 Lam, A. J., St-Pierre, F., Gong, Y., Marshall, J. D., Cranfill, P. J., Baird, M. A., McKeown, M.
839       R., Wiedenmann, J., Davidson, M. W., Schnitzer, M. J., Tsien, R. Y., & Lin, M. Z.
840       (2012). Improving FRET dynamic range with bright green and red fluorescent proteins.
841       *Nat Methods, 9*(10), 1005-1012. doi:10.1038/nmeth.2171

842 Leonetti, M. D., Sekine, S., Kamiyama, D., Weissman, J. S., & Huang, B. (2016). A scalable
843       strategy for high-throughput GFP tagging of endogenous human proteins. *Proc Natl Acad*
844       *Sci U S A, 113*(25), E3501-3508. doi:10.1073/pnas.1606731113

845   Lesage, S., Drouet, V., Majounie, E., Deramecourt, V., Jacoupy, M., Nicolas, A., Cormier-
846           Dequaire, F., Hassoun, S. M., Pujol, C., Ciura, S., Erpapazoglou, Z., Usenko, T.,
847           Maurage, C. A., Sahbatou, M., Liebau, S., Ding, J., Bilgic, B., Emre, M., Erginel-
848           Unaltuna, N., Guven, G., Tison, F., Tranchant, C., Vidailhet, M., Corvol, J. C., Krack, P.,
849           Leutenegger, A. L., Nalls, M. A., Hernandez, D. G., Heutink, P., Gibbs, J. R., Hardy, J.,
850           Wood, N. W., Gasser, T., Durr, A., Deleuze, J. F., Tazir, M., Destee, A., Lohmann, E.,
851           Kabashi, E., Singleton, A., Corti, O., Brice, A., French Parkinson's Disease Genetics, S.,
852           & International Parkinson's Disease Genomics, C. (2016). Loss of VPS13C Function in
853           Autosomal-Recessive Parkinsonism Causes Mitochondrial Dysfunction and Increases
854           PINK1/Parkin-Dependent Mitophagy. *Am J Hum Genet, 98*(3), 500-513.
855           doi:10.1016/j.ajhg.2016.01.014

856   Maejima, I., Takahashi, A., Omori, H., Kimura, T., Takabatake, Y., Saitoh, T., Yamamoto, A.,
857           Hamasaki, M., Noda, T., Isaka, Y., & Yoshimori, T. (2013). Autophagy sequesters
858           damaged lysosomes to control lysosomal biogenesis and kidney injury. *EMBO J, 32*(17),
859           2336-2347. doi:10.1038/emboj.2013.171

860   McKeith, I. G., Dickson, D. W., Lowe, J., Emre, M., O'Brien, J. T., Feldman, H., Cummings, J.,
861           Duda, J. E., Lippa, C., Perry, E. K., Aarsland, D., Arai, H., Ballard, C. G., Boeve, B.,
862           Burn, D. J., Costa, D., Del Ser, T., Dubois, B., Galasko, D., Gauthier, S., Goetz, C. G.,
863           Gomez-Tortosa, E., Halliday, G., Hansen, L. A., Hardy, J., Iwatsubo, T., Kalaria, R. N.,
864           Kaufer, D., Kenny, R. A., Korczyn, A., Kosaka, K., Lee, V. M., Lees, A., Litvan, I.,
865           Londos, E., Lopez, O. L., Minoshima, S., Mizuno, Y., Molina, J. A., Mukaetova-
866           Ladinska, E. B., Pasquier, F., Perry, R. H., Schulz, J. B., Trojanowski, J. Q., Yamada, M.,
867           & Consortium on, D. L. B. (2005). Diagnosis and management of dementia with Lewy
868           bodies: third report of the DLB Consortium. *Neurology, 65*(12), 1863-1872.
869           doi:10.1212/01.wnl.0000187889.17253.b1

870   Mirbaha, H., Holmes, B. B., Sanders, D. W., Bieschke, J., & Diamond, M. I. (2015). Tau
871           Trimers Are the Minimal Propagation Unit Spontaneously Internalized to Seed
872           Intracellular Aggregation. *J Biol Chem, 290*(24), 14893-14903.
873           doi:10.1074/jbc.M115.652693

874   Mok, S. A., Condello, C., Freilich, R., Gillies, A., Arhar, T., Oroz, J., Kadavath, H., Julien, O.,
875           Assimon, V. A., Rauch, J. N., Dunyak, B. M., Lee, J., Tsai, F. T. F., Wilson, M. R.,
876           Zweckstetter, M., Dickey, C. A., & Gestwicki, J. E. (2018). Mapping interactions with
877           the chaperone network reveals factors that protect against tau aggregation. *Nat Struct Mol
878           Biol, 25*(5), 384-393. doi:10.1038/s41594-018-0057-1

879   Montine, T. J., Phelps, C. H., Beach, T. G., Bigio, E. H., Cairns, N. J., Dickson, D. W.,
880           Duyckaerts, C., Frosch, M. P., Masliah, E., Mirra, S. S., Nelson, P. T., Schneider, J. A.,
881           Thal, D. R., Trojanowski, J. Q., Vinters, H. V., Hyman, B. T., National Institute on, A., &
882           Alzheimer's, A. (2012). National Institute on Aging-Alzheimer's Association guidelines
883           for the neuropathologic assessment of Alzheimer's disease: a practical approach. *Acta
884           Neuropathol, 123*(1), 1-11. doi:10.1007/s00401-011-0910-3

Nonaka, T., Watanabe, S. T., Iwatsubo, T., & Hasegawa, M. (2010). Seeded aggregation and toxicity of {alpha}-synuclein and tau: cellular models of neurodegenerative diseases. *J Biol Chem, 285*(45), 34885-34898. doi:10.1074/jbc.M110.148460

Prusiner, S. B. (1982). Novel proteinaceous infectious particles cause scrapie. *Science, 216*(4542), 136-144.

Rampoldi, L., Dobson-Stone, C., Rubio, J. P., Danek, A., Chalmers, R. M., Wood, N. W., Verellen, C., Ferrer, X., Malandrini, A., Fabrizi, G. M., Brown, R., Vance, J., Pericak-Vance, M., Rudolf, G., Carre, S., Alonso, E., Manfredi, M., Nemeth, A. H., & Monaco, A. P. (2001). A conserved sorting-associated protein is mutant in chorea-acanthocytosis. *Nat Genet, 28*(2), 119-120. doi:10.1038/88821

Rauch, J. N., Chen, J. J., Sorum, A. W., Miller, G. M., Sharf, T., See, S. K., Hsieh-Wilson, L. C., Kampmann, M., & Kosik, K. S. (2018). Tau Internalization is Regulated by 6-O Sulfation on Heparan Sulfate Proteoglycans (HSPGs). *Sci Rep, 8*(1), 6382. doi:10.1038/s41598-018-24904-z

Sanders, D. W., Kaufman, S. K., DeVos, S. L., Sharma, A. M., Mirbaha, H., Li, A., Barker, S. J., Foley, A. C., Thorpe, J. R., Serpell, L. C., Miller, T. M., Grinberg, L. T., Seeley, W. W., & Diamond, M. I. (2014). Distinct tau prion strains propagate in cells and mice and define different tauopathies. *Neuron, 82*(6), 1271-1288. doi:10.1016/j.neuron.2014.04.047

Schreij, A. M., Fon, E. A., & McPherson, P. S. (2016). Endocytic membrane trafficking and neurodegenerative disease. *Cell Mol Life Sci, 73*(8), 1529-1545. doi:10.1007/s00018-015-2105-x

Seong, E., Insolera, R., Dulovic, M., Kamsteeg, E. J., Trinh, J., Bruggemann, N., Sandford, E., Li, S., Ozel, A. B., Li, J. Z., Jewett, T., Kievit, A. J. A., Munchau, A., Shakkottai, V., Klein, C., Collins, C. A., Lohmann, K., van de Warrenburg, B. P., & Burmeister, M. (2018). Mutations in VPS13D lead to a new recessive ataxia with spasticity and mitochondrial defects. *Ann Neurol, 83*(6), 1075-1088. doi:10.1002/ana.25220

Skibinski, G., Parkinson, N. J., Brown, J. M., Chakrabarti, L., Lloyd, S. L., Hummerich, H., Nielsen, J. E., Hodges, J. R., Spillantini, M. G., Thusgaard, T., Brandner, S., Brun, A., Rossor, M. N., Gade, A., Johannsen, P., Sorensen, S. A., Gydesen, S., Fisher, E. M., & Collinge, J. (2005). Mutations in the endosomal ESCRTIII-complex subunit CHMP2B in frontotemporal dementia. *Nat Genet, 37*(8), 806-808. doi:10.1038/ng1609

Skowyra, M. L., Schlesinger, P. H., Naismith, T. V., & Hanson, P. I. (2018). Triggered recruitment of ESCRT machinery promotes endolysosomal repair. *Science, 360*(6384). doi:10.1126/science.aar5078

Small, S. A., Simoes-Spassov, S., Mayeux, R., & Petsko, G. A. (2017). Endosomal Traffic Jams Represent a Pathogenic Hub and Therapeutic Target in Alzheimer's Disease. *Trends Neurosci, 40*(10), 592-602. doi:10.1016/j.tins.2017.08.003

923 Stöhr, J., Wu, H., Nick, M., Wu, Y., Bhate, M., Condello, C., Johnson, N., Rodgers, J., Lemmin,
924      T., Acharya, S., Becker, J., Robinson, K., Kelly, M. J. S., Gai, F., Stubbs, G., Prusiner, S.
925      B., & DeGrado, W. F. (2017). A 31-residue peptide induces aggregation of tau's
926      microtubule-binding region in cells. *Nat Chem, 9*(9), 874-881. doi:10.1038/nchem.2754

927 Stopschinski, B. E., Holmes, B. B., Miller, G. M., Manon, V. A., Vaquer-Alicea, J., Prueitt, W.
928      L., Hsieh-Wilson, L. C., & Diamond, M. I. (2018). Specific glycosaminoglycan chain
929      length and sulfation patterns are required for cell uptake of tau versus alpha-synuclein
930      and beta-amyloid aggregates. *J Biol Chem, 293*(27), 10826-10840.
931      doi:10.1074/jbc.RA117.000378

932 Tartaglia, M. C., Sidhu, M., Laluz, V., Racine, C., Rabinovici, G. D., Creighton, K., Karydas, A.,
933      Rademakers, R., Huang, E. J., Miller, B. L., DeArmond, S. J., & Seeley, W. W. (2010).
934      Sporadic corticobasal syndrome due to FTLD-TDP. *Acta Neuropathol, 119*(3), 365-374.
935      doi:10.1007/s00401-009-0605-1

936 Thiele, D. L., & Lipsky, P. E. (1990). Mechanism of L-leucyl-L-leucine methyl ester-mediated
937      killing of cytotoxic lymphocytes: dependence on a lysosomal thiol protease, dipeptidyl
938      peptidase I, that is enriched in these cells. *Proc Natl Acad Sci U S A, 87*(1), 83-87.

939 Tian, R., Gachechiladze, M. A., Ludwig, C. H., Laurie, M. T., Hong, J. Y., Nathaniel, D.,
940      Prabhu, A. V., Fernandopulle, M. S., Patel, R., Ward, M. E., & Kampmann, M. (2019).
941      CRISPR-based platform for multimodal genetic screens in human iPSC-derived neurons.
942      *bioRxiv, 513309; doi:* https://doi.org/10.1101/513309.

943 Tsherniak, A., Vazquez, F., Montgomery, P. G., Weir, B. A., Kryukov, G., Cowley, G. S., Gill,
944      S., Harrington, W. F., Pantel, S., Krill-Burger, J. M., Meyers, R. M., Ali, L., Goodale, A.,
945      Lee, Y., Jiang, G., Hsiao, J., Gerath, W. F. J., Howell, S., Merkel, E., Ghandi, M.,
946      Garraway, L. A., Root, D. E., Golub, T. R., Boehm, J. S., & Hahn, W. C. (2017).
947      Defining a Cancer Dependency Map. *Cell, 170*(3), 564-576 e516.
948      doi:10.1016/j.cell.2017.06.010

949 Ueno, S., Maruki, Y., Nakamura, M., Tomemori, Y., Kamae, K., Tanabe, H., Yamashita, Y.,
950      Matsuda, S., Kaneko, S., & Sano, A. (2001). The gene encoding a newly discovered
951      protein, chorein, is mutated in chorea-acanthocytosis. *Nat Genet, 28*(2), 121-122.
952      doi:10.1038/88825

953 Urwin, H., Authier, A., Nielsen, J. E., Metcalf, D., Powell, C., Froud, K., Malcolm, D. S., Holm,
954      I., Johannsen, P., Brown, J., Fisher, E. M., van der Zee, J., Bruyland, M., Consortium, F.
955      R., Van Broeckhoven, C., Collinge, J., Brandner, S., Futter, C., & Isaacs, A. M. (2010).
956      Disruption of endocytic trafficking in frontotemporal dementia with CHMP2B mutations.
957      *Hum Mol Genet, 19*(11), 2228-2238. doi:10.1093/hmg/ddq100

958 Vaquer-Alicea, J., & Diamond, M. I. (2019). Propagation of Protein Aggregation in
959      Neurodegenerative Diseases. *Annu Rev Biochem*. doi:10.1146/annurev-biochem-061516-
960      045049

961 Velayos-Baeza, A., Vettori, A., Copley, R. R., Dobson-Stone, C., & Monaco, A. P. (2004).
962         Analysis of the human VPS13 gene family. *Genomics, 84*(3), 536-549.
963         doi:10.1016/j.ygeno.2004.04.012

964 Voss, K., Combs, B., Patterson, K. R., Binder, L. I., & Gamblin, T. C. (2012). Hsp70 alters tau
965         function and aggregation in an isoform specific manner. *Biochemistry, 51*(4), 888-898.
966         doi:10.1021/bi2018078

967 Wang, Y., & Mandelkow, E. (2016). Tau in physiology and pathology. *Nat Rev Neurosci, 17*(1),
968         5-21. doi:10.1038/nrn.2015.1

969 Woerman, A. L., Aoyagi, A., Patel, S., Kazmi, S. A., Lobach, I., Grinberg, L. T., McKee, A. C.,
970         Seeley, W. W., Olson, S. H., & Prusiner, S. B. (2016). Tau prions from Alzheimer's
971         disease and chronic traumatic encephalopathy patients propagate in cultured cells. *Proc*
972         *Natl Acad Sci U S A, 113*(50), E8187-E8196. doi:10.1073/pnas.1616344113

973 Yan, X., Uronen, R. L., & Huttunen, H. J. (2018). The interaction of alpha-synuclein and Tau: A
974         molecular conspiracy in neurodegeneration? *Semin Cell Dev Biol*.
975         doi:10.1016/j.semcdb.2018.05.005

976 Yeshaw, W. M., van der Zwaag, M., Pinto, F., Lahaye, L. L., Faber, A. I., Gomez-Sanchez, R.,
977         Dolga, A. M., Poland, C., Monaco, A. P., van, I. S. C., Grzeschik, N. A., Velayos-Baeza,
978         A., & Sibon, O. C. (2019). Human VPS13A is associated with multiple organelles and
979         influences mitochondrial morphology and lipid droplet motility. *Elife, 8*.
980         doi:10.7554/eLife.43561

981 Young, Z. T., Mok, S. A., & Gestwicki, J. E. (2018). Therapeutic Strategies for Restoring Tau
982         Homeostasis. *Cold Spring Harb Perspect Med, 8*(1). doi:10.1101/cshperspect.a024612

983 Zhou, X., & Huang, L. (1994). DNA transfection mediated by cationic liposomes containing
984         lipopolylysine: characterization and mechanism of action. *Biochim Biophys Acta,*
985         *1189*(2), 195-203.
986

**SUPPLEMENTAL TABLE AND MOVIE LEGENDS**

**Table S1 – Gene epsilon and p values for CRISPRi screens**

Excel spreadsheet containing the combined analyzed results for the CRISPRi screens performed with the Proteostasis-focused sgRNA libraries. The counts for each library screen were analyzed using our MaGecK-iNC pipeline (see materials and methods). (**Tab 1**) The columns list the gene index, epsilon (phenotype, where negative valudes indicate less aggregation, positive values indicate more aggregation, p-value, product (epsilon*–log10 p-value), and gene name. NTC indicate "quasi-genes" composed of random sets of 5 non-targeting negative control sgRNAs.

**Table S2 – sgRNA sequences and validation**

(**Tabs 1-3**) List of sgRNA targets and accompanying protospacers used for CRISPRi screens. The columns list the target and protospacer. (Tab 1) Endolysosome/Autophagy (Tab 2) Chaperones/Co-chaperonse (Tab 3) Ubiquitin Proteasome System. (**Tab 1,2**) Validation of target gene knockdown by CRISPRi. (Tab 4) Columns list sgRNA activity, which is expressed as percent knockdown, standard error from n=3 technical replicates, and sgRNA oligos used in experiments for single sgRNA analysis. The columns list the sgRNA, % knockdown efficiency, standard error from n=3 technical replicates, forward oligo, and reverse oligos (used for generating lentiviral sgRNA expression plasmids. (Tab 4) Oligonucleotides used for RT-qPCR analysis. The columns list the gene target, forward, and reverse primer.

**Supplemental Movie 1 – Time-lapse of tau aggregate formation in HEK293T cells expressing tau.K18(LM)-Clover2 and transduced with non-targeting control sgRNA**

Time-lapse microscopy of cell entry of AF555-tau fibrils and resulting aggregation of the cytosolic tau-clover2 construct. CRISPRi-HEK293T cells expressing tau.K18(LM)-clover2 transduced with a non-targeting control. Each frame represents 20 minute intervals and is played at 5 frames per second; movie starts with the addition of fibrils.

**Supplemental Movie 2 - Time-lapse of tau aggregate formation in HEK293T cells expressing tau.K18(LM)-Clover2 and transduced with CHMP6 sgRNA**

1017    Time-lapse microscopy of cell entry of AF555-tau fibrils and resulting aggregation of the

1018    cytosolic tau-clover2 construct. CRISPRi-HEK293T cells expressing tau.K18(LM)-clover2

1019    transduced with a CHMP6 sgRNA. Each frame represents 20 minute intervals and is played at 5

1020    frames per second; movie starts with the addition of fibrils.

1021

1022    **Supplemental Movie 3 – Time-lapse of AF555-tau fibrils in cells expressing tagged mNG$_{11}$-**

1023    **RAB7A**

1024    Time-lapse microscopy of partial co-localization of AF555-tau fibrils with RAB7A tagged

1025    vesicles. HEK293T cells with tagged mNG$_{11}$-RAB7A were treated with AF555-tau fibrils for 22

1026    hours before movies were acquired. Each frame represents 2.4 second intervals and is played at 5

1027    frames per second.

1028

1029    **Supplemental Movie 4 – Time-lapse of AF555-tau fibrils in cells expressing tagged mNG$_{11}$-**

1030    **LAMP1**

1031    Time-lapse microscopy of partial co-localization of AF555-tau fibrils with RAB7A tagged

1032    vesicles. HEK293T cells with tagged mNG$_{11}$-LAMP1 were treated with AF555-tau fibrils for 22

1033    hours before movies were acquired. Each frame represents 2.4 second intervals and is played at 5

1034    frames per second.